

THE TRANSIT LIGHT SOURCE EFFECT: FALSE SPECTRAL FEATURES AND INCORRECT DENSITIES FOR M-DWARF TRANSITING PLANETS

BENJAMIN V. RACKHAM,^{1,2,3} DÁNIEL APAI,^{1,4,3} AND MARK S. GIAMPAPA⁵

¹Department of Astronomy/Steward Observatory, The University of Arizona, 933 N. Cherry Avenue, Tucson, AZ 85721, USA

²National Science Foundation Graduate Research Fellow.

³Earths in Other Solar Systems Team, NASA Nexus for Exoplanet System Science.

⁴Department of Planetary Sciences, The University of Arizona, 1629 E. University Blvd, Tucson, AZ 85721, USA

⁵National Solar Observatory, 950 N. Cherry Avenue, Tucson, AZ 85719, USA

(Received Oct. 4, 2017; Revised Dec. 5, 2017; Accepted Dec. 6, 2017)

ABSTRACT

Transmission spectra are differential measurements that utilize stellar illumination to probe transiting exoplanet atmospheres. Any spectral difference between the illuminating light source and the disk-integrated stellar spectrum due to starspots and faculae will be imprinted in the observed transmission spectrum. However, few constraints exist for the extent of photospheric heterogeneities in M dwarfs. Here, we model spot and faculae covering fractions consistent with observed photometric variabilities for M dwarfs and the associated 0.3–5.5 μ m stellar contamination spectra. We find that large ranges of spot and faculae covering fractions are consistent with observations and corrections assuming a linear relation between variability amplitude and covering fractions generally underestimate the stellar contamination. Using realistic estimates for spot and faculae covering fractions, we find stellar contamination can be more than 10 \times larger than transit depth changes expected for atmospheric features in rocky exoplanets. We also find that stellar spectral contamination can lead to systematic errors in radius and therefore the derived density of small planets. In the case of the TRAPPIST-1 system, we show that TRAPPIST-1’s rotational variability is consistent with spot covering fractions $f_{spot} = 8^{+18}_{-7}\%$ and faculae covering fractions $f_{fac} = 54^{+16}_{-46}\%$. The associated stellar contamination signals alter transit depths of the TRAPPIST-1 planets at wavelengths of interest for planetary atmospheric species by roughly 1–15 \times the strength of planetary features, significantly complicating *JWST* follow-up observations of this system. Similarly, we find that stellar contamination can lead to underestimates of bulk densities of the TRAPPIST-1 planets of $\Delta(\rho) = -3^{+3}_{-8}\%$, thus leading to overestimates of their volatile contents.

Keywords: methods: numerical, planets and satellites: atmospheres, fundamental parameters, stars: activity, starspots, techniques: spectroscopic

1. INTRODUCTION

Transmission spectroscopy, the multi-wavelength study of transits that reveals the apparent size of the exoplanet as a function of wavelength (e.g., Seager & Sasselov 2000; Brown 2001), provides the best opportunity to study the atmospheres of small and cool exoplanets in the coming decades. During a transit, exoplanets appear larger at some wavelengths due to absorption or scattering of starlight by their atmospheres. The scale of the signal depends inversely on the square of the stellar radius (Miller-Ricci et al. 2009), prompting a focus on studying exoplanets around M dwarf stars.

A rapidly growing number of exciting M dwarf exoplanet systems hosting super-Earth and Earth-mass planets have been discovered to date, including GJ 1132b (Berta-Thompson et al. 2015), LHS 1140b (Dittmann et al. 2017), and the TRAPPIST-1 system (Gillon et al. 2016, 2017; Luger et al. 2017), an ultracool dwarf only 12 parsecs away hosting a system of seven transiting Earth-sized planets. The low densities of the TRAPPIST-1 planets may indicate high volatile contents, and as many as three of them may have surface temperatures temperate enough for long-lived liquid water to exist (Gillon et al. 2017). Frequent flaring (Vida et al. 2017) and strong XUV radiation from the host star (Wheatley et al. 2017), however, can lead to significant water loss for these planets (Bolmont et al. 2017), and 3D climate modeling suggests TRAPPIST-1e provides the best opportunity for present-day surface water and an Earth-like temperature in the system (Wolf 2017).

While M dwarf exoplanets provide an excellent opportunity to study small and cool exoplanets (Barstow & Irwin 2016), they also represent a significant challenge. Spots with covering fractions as low as 1% on M dwarfs introduce radial velocity jitter that can mask the presence of habitable zone Earth-sized exoplanets (Andersen & Korhonen 2015). Variability monitoring suggests 1–3% of M dwarfs have spot covering fractions of 10% or more (Goulding et al. 2012). In addition to radial velocity jitter, unocculted spots also introduce errors in wavelength-dependent planetary radii recovered from transit observations (e.g., Pont et al. 2008). Given the dependence of density calculations on measurements of exoplanet radii ($\rho \propto R^{-3}$), any errors in radius determinations are amplified by a factor of 3 in the estimate of the exoplanet bulk density and can lead to significant consequences for the development of accurate exoplanet models.

Unocculted spots are one manifestation of a generic issue with transit observations that we term the *transit light source effect* (Figure 1): Any transmission spectroscopic measurement relies on measuring the difference

between the *incident* and *transmitted* light to identify the absorbers present in the media studied (e.g., Seager & Sasselov 2000). The level of accuracy with which the incident spectrum is known will directly determine the level of accuracy with which the transmitted light is understood. In the transiting exoplanet case, the incident light is measured by observing the disk-integrated stellar spectrum before the transit (e.g., Brown 2001), the assumption being that the disk-integrated spectrum is identical to the light incident on the planetary atmosphere. However, this is only an approximation: the planet is not occulting the entire stellar disk but only a small region within the transit chord at a given time. Thus, the light source for the transmission measurement is a small time-varying annulus within the stellar disk defined by the planet’s projection, the spectrum of which may differ significantly from the disk-averaged spectrum. Such differences are expected due to the fact that stellar atmospheres are rarely perfectly homogeneous, as illustrated by spatially resolved observations of the Sun (e.g., Llama & Shkolnik 2015, 2016). Cool stellar spots (umbra and penumbra), hot faculae, and even latitudinal temperature gradients will result in a spectral mismatch, even if some of these will not be evident in broad-band photometric light curves.

The Sun displays a clear latitudinal dependence of active regions that gives rise to the so-called butterfly diagram (Maunder 1922; Babcock 1961; Mandal et al. 2017). Transiting exoplanets have been proposed to be tools to probe the latitudinal and temporal distributions of active regions in other stars (Dittmann et al. 2009; Llama et al. 2012). High-resolution transit observations can be used to spatially resolve the emergent stellar spectrum along the transit path of the planet (Cauley et al. 2017; Dravins et al. 2017a,b). Morris et al. (2017) recently utilized the highly misaligned exoplanet HAT-P-11b to probe the starspot radii and latitudinal distribution of its K4 dwarf host star and found that, much like the Sun, spots on HAT-P-11 emerge preferentially at two low latitudes. In general, however, orbital planes of transiting exoplanets tend to be more aligned with stellar rotation axes than that of HAT-P-11b, displaying obliquities of $\lesssim 20^\circ$ (Winn et al. 2017). To complicate matters further, unlike the Sun and HAT-P-11, M dwarfs may exhibit spots at all latitudes (Barnes et al. 2001). Thus, stellar latitudes sampled by transit chords may not provide a representative picture of photospheric active regions.

Correcting transmission spectra for photospheric heterogeneities within the transit chord, such as spots (e.g., Pont et al. 2013; Llama & Shkolnik 2015) and faculae (Oshagh et al. 2014), is possible, provided they are large

The Transit Light Source Effect

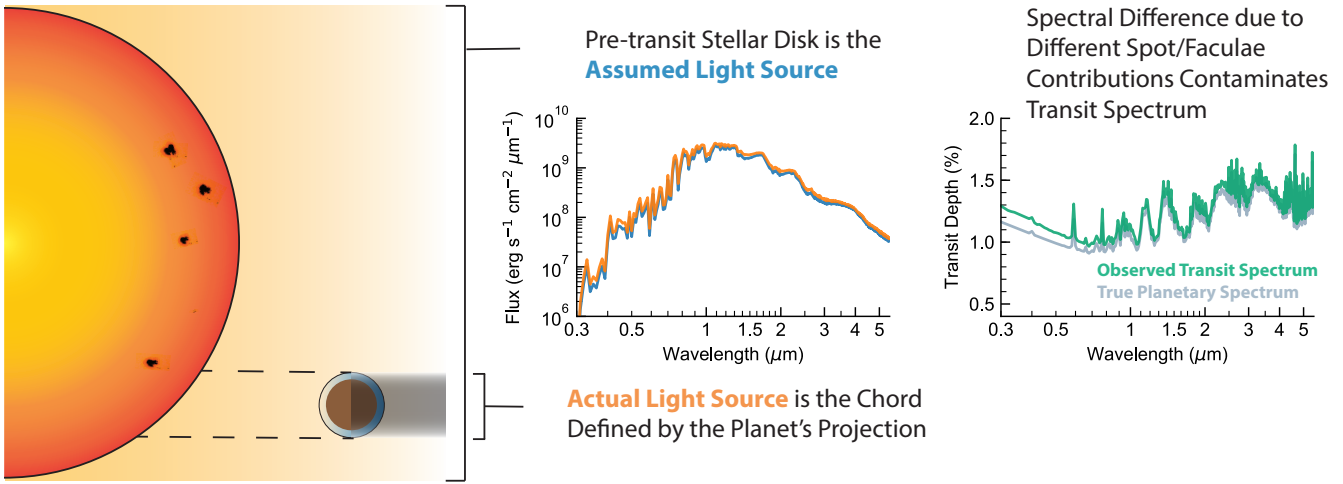


Figure 1. A Schematic of the Transit Light Source Effect. During a transit, exoplanet atmospheres are illuminated by the portion of a stellar photosphere immediately behind the exoplanet from the point of view of the observed. Changes in transit depth must be measured relative to the spectrum of this light source. However, the light source is generally assumed to be the disk-integrated spectrum of the star. Any differences between the assumed and actual light sources will lead to apparent variations in transit depth.

enough to produce an observable change in the light curve during the transit. Modulations in the shape of the transit light curve can be used to constrain the temperature (Sing et al. 2011) and size (Béky et al. 2014) of the occulted photospheric feature, which determine its contribution to the transmission spectrum, or more simply, time points including the crossing event may be excluded from the transit fit (e.g., Pont et al. 2008; Carter et al. 2011; Narita et al. 2013).

Unocculted heterogeneities, however, represent a more pathological manifestation of the transit light source effect because they do not produce temporal changes in the observed light curve. Previous attempts to correct for unocculted photospheric features have largely relied on photometric monitoring of the exoplanet host star to ascertain the extent of photospheric heterogeneities present (Pont et al. 2008, 2013; Berta et al. 2011; Désert et al. 2011; Sing et al. 2011; Knutson et al. 2012; Narita et al. 2013; Nascimbeni et al. 2015; Zellem et al. 2015). This approach is limited in two respects: 1) rotational variability monitoring traces only the non-axisymmetric component of the stellar heterogeneity (Jackson & Jeffries 2012), i.e., any persistent, underlying level of heterogeneity will not be detectable with variability monitoring; and 2) the source of the variability is commonly assumed to be a single giant spot, the size of which scales linearly with the variability amplitude, an assumption which provides only a lower limit on the extent of active regions.

Zellem et al. (2017) present a novel method to remove relative changes in the stellar contribution to individual transits utilizing the out-of-transit data flanking each transit observation. The strength of this approach lies in that it does not require additional measurements to provide a relative correction for differences in spot and faculae covering fractions between observations. However, as with other variability-based techniques, this approach cannot correct for any persistent level of spots or faculae that may be present in all observations and can strongly alter transmission spectra (McCullough et al. 2014; Rackham et al. 2017).

Useful constraints on spot and faculae covering fractions are hindered by observational and theoretical limits on our knowledge of stellar photospheres. On the Sun, the disk passage of sunspots can produce relative declines in the solar total irradiance in the range of $\sim 0.1\%$ to 0.3% (e.g., Kopp et al. 2005). By contrast, field mid-to-late M dwarfs ($M < 0.35 M_{\odot}$) with detectable rotation periods display rotational modulations with semi-amplitudes of $0.5\text{--}1.0\%$ (Newton et al. 2016), corresponding to peak-to-trough variability full-amplitudes of $1\text{--}2\%$. Thus, variability amplitudes in M dwarfs are roughly an order of magnitude larger than in the Sun.

Despite the clear importance of constraining spot and faculae covering fractions for exoplanet host stars, a systematic attempt to connect observed variabilities to covering fractions and thus stellar contamination signals is absent in the literature on transmission spectroscopy.

In this work, we employ a forward modeling approach to explore the range of spot covering fractions consistent with observed photometric variabilities for field M dwarf stars and their associated effects on visual and near-infrared (0.3–5.5 μm) planetary transmission spectra. In Section 2, we detail our model for placing constraints on spot and faculae covering fractions and their associated stellar contamination spectra. Section 3 provides the modeling results. We place our results in the context of observational attempts to constrain stellar heterogeneity and examine their impact on transmission spectra and density estimates of M dwarf exoplanets in Section 4, including a focused discussion of the TRAPPIST-1 system. Finally, we summarize our conclusions in Section 5.

2. METHODS

2.1. Synthetic stellar spectra

We employed the PHOENIX (Husser et al. 2013) and DRIFT-PHOENIX (Witte et al. 2011) stellar spectral model grids to generate spectra for the immaculate photospheres, spots, and faculae of main sequence M dwarfs with spectral types from M0V to M9V. Both model grids are based on the stellar atmosphere code PHOENIX (Hauschildt & Baron 1999), with the DRIFT-PHOENIX model grids including additional physics describing the formation and condensation of mineral dust clouds (Woitke & Helling 2003, 2004; Helling & Woitke 2006; Helling et al. 2008a,b; Witte et al. 2009) that is applicable to late M dwarfs and brown dwarfs. We considered models with solar metallicity ($[\text{Fe}/\text{H}] = 0.0$) and no alpha-element enrichment ($[\alpha/\text{Fe}] = 0.0$). We linearly interpolated between spectra in the grids to produce 0.3–5.5 μm model spectra for the surface gravities and temperatures we required.

The implicit assumption with this approach is that the emergent spectrum from distinct components of a stellar photosphere, such as the immaculate photosphere, spots, and faculae, can be approximated by models of disk-integrated stellar spectra of different temperatures. This approximation is commonly used in transit spectroscopy studies to constrain the contribution of unocculted photospheric heterogeneities to exoplanet transmission spectra (Pont et al. 2008; Sing et al. 2011; Huitson et al. 2013; Jordán et al. 2013; Pont et al. 2013; Fraine et al. 2014; Sing et al. 2016; Rackham et al. 2017). However, this simplification neglects the dependence of the spectra of photospheric heterogeneities on magnetic field strength and limb distance, both of which modulate the emergent spectra of magnetic surface features (Norris et al. 2017). Nonetheless, we adopt the simplifying assumption of parameterizing component spectra by temperature and note that future efforts may benefit

Table 1. Adopted stellar parameters

Sp. Type	T_{phot} (K)	T_{spot} (K)	T_{fac} (K)	$\log g$ (cgs)
M0V	3800	3268	3900	4.7
M1V	3600	3096	3700	4.7
M2V	3400	2924	3500	4.8
M3V	3250	2795	3350	4.9
M4V	3100	2666	3200	5.3
M5V	2800	2408	2900	5.4
M6V	2600	2236	2700	5.6
M7V	2500	2150	2600	5.6
M8V	2400	2064	2500	5.7
M9V	2300	1978	2400	5.6

NOTE—The photosphere temperature T_{phot} , spot temperature T_{spot} , facula temperature T_{fac} , and surface gravity $\log g$ we adopt for each M dwarf spectral type are listed.

from the increased realism of 3D magnetohydrodynamics models.

Table 1 lists our adopted stellar parameters. For each spectral type, we calculated the surface gravity g from the stellar masses and radii summarized by Kaltenegger & Traub (2009) and adopted the stellar effective temperature from that same work as the photosphere temperature T_{phot} . Following Afram & Berdyugina (2015), we adopted the relation $T_{\text{spot}} = 0.86 \times T_{\text{phot}}$, in which T_{spot} is the spot temperature. We adopted the scaling relation $T_{\text{fac}} = T_{\text{phot}} + 100$ K (Gondoin 2008) for the facula temperature. Although there are uncertainties in the scaling relations of starspots and faculae, we do not expect our general results to be sensitive to the adopted relations. The temperature ranges of the spectral grids allowed us to simulate photosphere, spot, and facula spectra for spectral types M0V–M5V with the PHOENIX model grid and M5V–M9V with the DRIFT-PHOENIX model grid.

2.2. Spot covering fraction and variability amplitude relation

We explored the range of spot covering fractions consistent with an observed 1% I-band variability full-amplitude for each spectral type. We modeled the stellar photosphere using a rectangular grid with a resolution of 180×360 pixels. We initialized the model with an immaculate photosphere, setting the value of each resolution element to the flux of the photosphere spectrum

integrated over Bessel I-band response¹. Likewise, when adding spots or faculae to the model, we utilized the integrated I-band fluxes of their respective spectra.

We considered four cases of stellar heterogeneities by varying two parameters: spot size and the presence or absence of faculae. In terms of spot size, we examined cases with smaller and larger spots, which we deem the “solar-like spots” and “giant spots” cases. In the solar-like spots case, each spot had a radius of $R_{spot} = 2^\circ$, covering 400 ppm of the projected hemisphere and representing a large spot group on the Sun (Mandal et al. 2017). In the giant spots case, each spot had a radius of $R_{spot} = 7^\circ$, covering 5,000 ppm of the projected hemisphere and corresponding roughly to the largest spots detectable on active M dwarfs through molecular spectropolarimetry (Berdyugina 2011). For cases with faculae, we included faculae at a facula-to-spot area ratio of 10:1, following observations of the active Sun (Shapiro et al. 2014). Thus, the stellar heterogeneity cases we considered were the following: solar-like spots, giant spots, solar-like spots with faculae, and giant spots with faculae.

For each spectral type and stellar heterogeneity case, we examined the dependence of the variability on the spot covering fraction through an iterative process. In each iteration, we added a spot to the model photosphere at a randomly selected set of coordinates², recorded the spot covering fraction, and generated a phase curve. In cases including faculae, we added half of the facular area at positions adjacent to the spot and half in a roughly circular area at another randomly selected set of coordinates. We allowed spots to overwrite faculae but not vice versa in successive iterations to ensure the spot covering fraction increased monotonically. We generated a phase curve by applying a double cosine weighting kernel to one hemisphere of the rectangular grid (180×180 pixels), summing the flux, and repeating the process for all 360 x-coordinates (“latitudes”) in the model (Figure 2). We recorded the variability full-amplitude A as the difference between the minimum and maximum normalized flux in the phase curve at each iteration. This approach assumes the stellar rotation axis is aligned well with the plane of the sky. As the presence of transits ensures that the planetary orbital plane

is nearly edge-on, and obliquities between the stellar rotation axis and planetary orbital plane are generally $\lesssim 20^\circ$ (Winn et al. 2017), this assumption is good for most transiting exoplanet systems. Following this procedure, we added spots to the immaculate photosphere iteratively until reaching 50% spot coverage.

We repeated this procedure 100 times for a given set of stellar parameters and heterogeneity case to examine the central tendency and dispersion in modeling results. In each trial, we recorded the minimum spot covering fraction that produced a variability full-amplitude of 1% ($A = 0.01$). Using the results of the 100 trials, we calculated the mean spot covering fraction $f_{spot,mean}$ corresponding to $A = 0.01$ and its standard deviation. We defined the spot covering fractions 1σ below and above the mean as $f_{spot,min}$ and $f_{spot,max}$, respectively.

As spots were allowed to overwrite faculae in our model but not vice versa, the facula-to-spot area ratio drifted from its original 10:1 value as spots were added to the model. Thus a distribution of facular-covering fractions existed for each spot covering fraction of interest. Accordingly, to quantify the central tendency and dispersion in results for models including faculae, we calculated the mean and standard deviation of facular-covering fractions in the 100 trials for each spot covering fraction of interest. We defined $f_{fac,mean}$ as the mean facular-covering fraction corresponding to $f_{spot,mean}$, $f_{fac,min}$ as the mean facular-covering fraction corresponding to $f_{spot,min}$ minus one standard deviation of that distribution, and $f_{fac,max}$ as the mean facular-covering fraction corresponding to $f_{spot,max}$ plus one standard deviation of that distribution.

2.3. Model for stellar contamination spectra

Using the spot and faculae covering fractions determined through our variability modeling, we modeled the effect of stellar heterogeneity on observations of visual and near-infrared (0.3–5.5 μm) exoplanet transmission spectra. We utilized the Composite Photosphere and Atmospheric Transmission (CPAT) model described in Rackham et al. (2017) and the spectra described in Section 2.1. Recasting Equation (11) of Rackham et al. (2017) in terms of transit depths and simplifying terms, we find

$$D_{\lambda,obs} = \frac{D_\lambda}{1 - f_{het}(1 - \frac{F_{\lambda,het}}{F_{\lambda,phot}})}, \quad (1)$$

in which $D_{\lambda,obs}$ is the observed transit depth, D_λ is the nominal transit depth (i.e., the square of the true wavelength-dependent planet-to-star radius ratio), $F_{\lambda,phot}$ is the spectrum of the photosphere, $F_{\lambda,het}$ is the spectrum of a photospheric heterogeneity (i.e., spots or faculae), and f_{het} is the fraction of the projected stellar

¹ <http://www.aip.de/en/research/facilities/stella/instruments/data/johnson-ubvri-filter-curves>

² We assumed no latitudinal dependence for the spot distribution. This assumption is good for active M dwarf stars (Barnes et al. 2001; Barnes & Collier Cameron 2001), but may not hold for earlier spectral types (Morris et al. 2017). We will examine the additional complication of latitudinal dependence of photospheric features in a future paper.

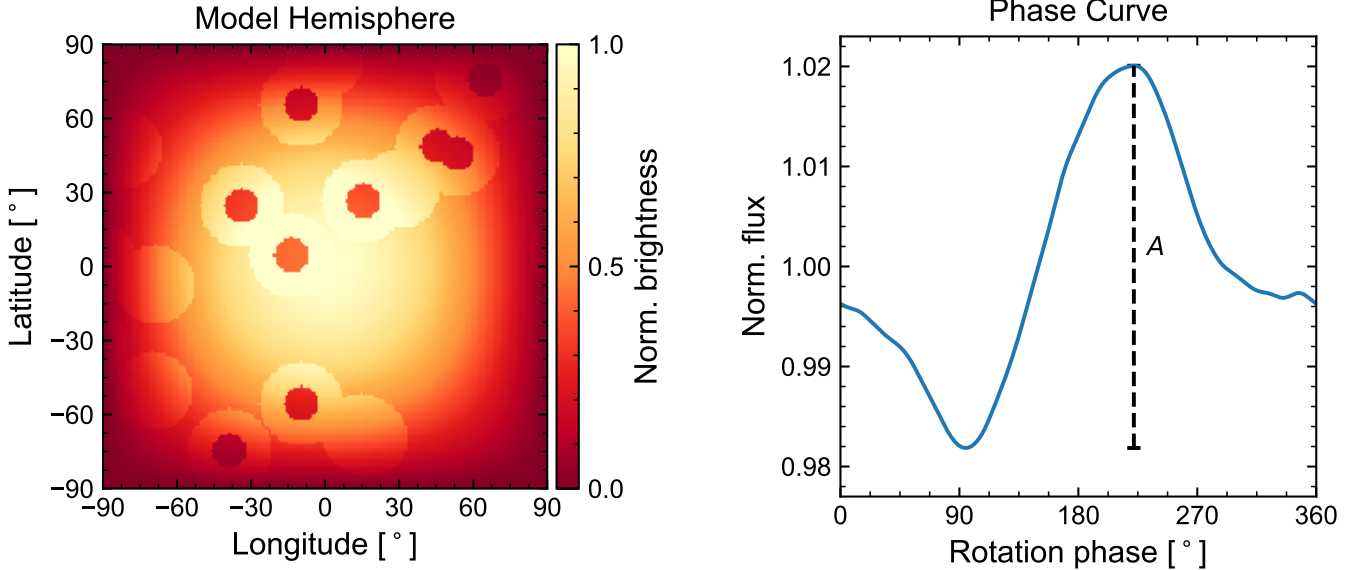


Figure 2. Example of a model stellar photosphere and variability amplitude determination. The left panel shows one hemisphere of an example model photosphere with giant spots and faculae regions after applying a double cosine weighting kernel. The right panel displays the phase curve produced by summing the hemispheric flux over one complete rotation of the model. The vertical dashed line illustrates the variability full-amplitude A , defined as the difference between the maximum and minimum normalized flux, which is $\sim 4\%$ in this case.

disk covered by the heterogeneity (see also McCullough et al. 2014, Equation (1)). This formalism assumes the transit chord can be described well by $F_{\lambda,phot}$, which is the case for transits of an immaculate photosphere. It also applies to transit observations in which the amplitude of the spot- or faculae-crossing event is larger than the observational uncertainty, thus enabling the parameters of the photospheric heterogeneity to be modeled (e.g., Sanchis-Ojeda & Winn 2011; Huitson et al. 2013; Pont et al. 2013; Tregloan-Reed et al. 2013; Scandariato et al. 2017) or the affected portion of the light curve to be removed from the analysis (e.g., Pont et al. 2008; Carter et al. 2011; Narita et al. 2013).

The denominator on the right side of Equation (1) represents the signal imprinted on the observed transit depth by the stellar heterogeneity. It is a multiplicative change to the transit depth independent of the exoplanet transmission spectrum. Therefore, by dividing Equation (1) by D_{λ} , we can define the term

$$\epsilon_{\lambda,het} = \frac{1}{1 - f_{het}(1 - \frac{F_{\lambda,het}}{F_{\lambda,phot}})}, \quad (2)$$

which we refer to as the contamination spectrum hereafter. Approaching the problem in this way allows contamination spectra to be calculated for different stellar parameters and applied to any exoplanetary transmission spectrum of interest.

Equation (2) holds when the stellar disk can be described by two spectral components (i.e., immaculate

photosphere and spots). In the case that spots and faculae are present in the stellar disk, the expression becomes

$$\epsilon_{\lambda,s+f} = \frac{1}{1 - f_{spot}(1 - \frac{F_{\lambda,spot}}{F_{\lambda,phot}}) - f_{fac}(1 - \frac{F_{\lambda,fac}}{F_{\lambda,phot}})}, \quad (3)$$

in which the $\epsilon_{\lambda,s+f}$ is the contamination spectrum produced by the combination of unocculted spots and faculae regions and the subscripts “spot” and “fac” refer to spots and faculae, respectively.

3. RESULTS

3.1. Spot covering fraction and variability amplitude relation

We find that, for all M dwarf spectral types, an observed variability full-amplitude corresponds to a typically wide range of spot covering fractions. Averaging over all spectral types, Table 2 provides a summary of the key results by heterogeneity case, including the spot and faculae covering fractions consistent with a 1% variability full-amplitude, the average transit depth change over the full wavelength range studied, and the primary contributor (spots or faculae) to the stellar contamination spectrum.

For a given variability, we find that the spot covering fraction depends strongly on the spot size. Figure 3 illustrates the origin of this dependence using two examples of model photospheres with $f_{spot} = 3\%$. For

Table 2. Summary of variability modeling results by heterogeneity case

Model Parameter	Heterogeneity Case			
	Giant Spots	Solar-like Spots	Giant Spots + Faculae	Solar-like Spots + Faculae
Spot covering fraction, $f_{spot}(\%)$	$0.9^{+1.3}_{-0.4}$	12^{+23}_{-6}	$0.5^{+0.8}_{-0.1}$	14^{+16}_{-7}
Faculae covering fraction, $f_{fac}(\%)$	-	-	$4.6^{+7.4}_{-1.4}$	63^{+5}_{-25}
Average transit depth change, $\bar{\epsilon}$ (%)	0.4	5.0	-0.4	5.8
Primary contributor to contamination spectrum	Spots	Spots	Faculae	Spots

NOTE—Here we summarize key results from the four cases of stellar photosphere heterogeneities that we considered (see Section 2.2). For each heterogeneity case, we provide the mean covering fractions of spots (and faculae, if possible) consistent with a 1% I-band rotational variability across all spectral types considered. The error bars on these values refer to the means of the $f_{spot,min}$, $f_{spot,max}$, $f_{fac,min}$, and $f_{fac,max}$ parameters defined in Section 2.2. Also included is the average transit depth change produced by all models across the 0.3–5.5 μ m wavelength range and a qualitative assessment of the photospheric heterogeneity that dominates the contamination spectrum.

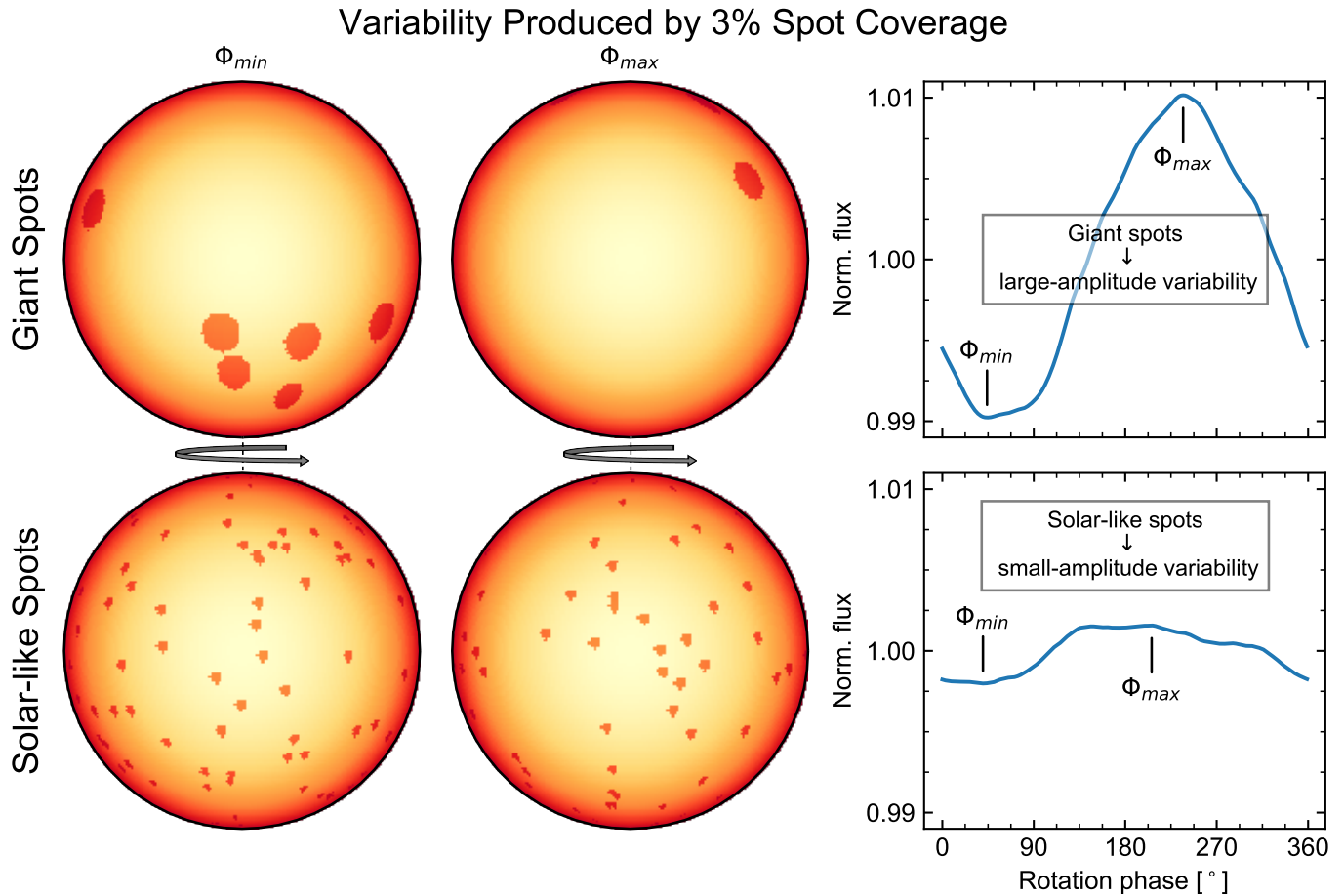


Figure 3. Illustration of dependence of variability on spot size. The case of giant (solar-like) spots is shown on the top (bottom) row. Both cases include 3% spot coverage. The stellar hemispheres corresponding to the minima (maxima) of the phase curves are shown in the left (center) column. The right column shows the phase curves for the two cases, and the phases of illustrated hemispheres are indicated.

Table 3. Filling factors and scaling coefficients determined by spots-only models

Sp. Type	Model Grid	$f_{spot,min}$	$f_{spot,mean}$	$f_{spot,max}$	C^a
Giant Spots					
M0V	PHOENIX	0.007	0.011	0.026	0.084 ± 0.030
M1V	PHOENIX	0.006	0.011	0.029	0.092 ± 0.036
M2V	PHOENIX	0.006	0.011	0.028	0.104 ± 0.041
M3V	PHOENIX	0.006	0.010	0.022	0.100 ± 0.038
M4V	PHOENIX	0.005	0.008	0.019	0.105 ± 0.043
M5V	PHOENIX	0.006	0.010	0.023	0.092 ± 0.035
M5V	DRIFT-PHOENIX	0.005	0.008	0.019	0.116 ± 0.041
M6V	DRIFT-PHOENIX	0.005	0.008	0.015	0.106 ± 0.040
M7V	DRIFT-PHOENIX	0.006	0.008	0.023	0.106 ± 0.040
M8V	DRIFT-PHOENIX	0.006	0.009	0.023	0.106 ± 0.041
M9V	DRIFT-PHOENIX	0.005	0.009	0.021	0.107 ± 0.042
Solar-like Spots					
M0V	PHOENIX	0.10	0.20	0.50	0.022 ± 0.009
M1V	PHOENIX	0.08	0.17	0.46	0.024 ± 0.009
M2V	PHOENIX	0.07	0.12	0.42	0.027 ± 0.011
M3V	PHOENIX	0.06	0.10	0.30	0.029 ± 0.010
M4V	PHOENIX	0.05	0.11	0.30	0.028 ± 0.010
M5V	PHOENIX	0.07	0.11	0.43	0.027 ± 0.010
M5V	DRIFT-PHOENIX	0.05	0.09	0.25	0.032 ± 0.012
M6V	DRIFT-PHOENIX	0.06	0.13	0.28	0.029 ± 0.010
M7V	DRIFT-PHOENIX	0.06	0.11	0.30	0.030 ± 0.011
M8V	DRIFT-PHOENIX	0.05	0.11	0.30	0.028 ± 0.011
M9V	DRIFT-PHOENIX	0.06	0.10	0.28	0.028 ± 0.010

^aScaling coefficient for square root scaling relation (Equation 4)

NOTE—Section 2.2 provides the definitions of the spot covering fractions $f_{spot,min}$, $f_{spot,mean}$, and $f_{spot,max}$.

a given spot covering fraction, the number density of spots is lower in the giant spots case than the solar-like spots case, leading to more concentrated surface heterogeneities and larger variability signals. A single spot, for example, will always lead to rotational variability, while the variability signals from multiple spots positioned around the photosphere can add destructively, leading to a lower observed variability full-amplitude. The solar-like spots case demonstrates this effect. It includes the same spot covering fraction as the giant spots case but produces a markedly lower level of variability. While chromospheric diagnostics may be used to distinguish active and quiet stars, variability monitoring can only place a lower limit on the spot covering fraction. In effect, the rotational variability full-amplitude reflects only the non-axisymmetric component of the stellar heterogeneity. The axisymmetric component, which can be larger than the non-axisymmetric one, does not contribute to the observed variability but will affect transmission spectra.

Figure 4 shows the results of our variability amplitude modeling efforts for the spots-only case. For each spectral type and spot size, the relationship between the spot covering fraction and observed I-band variability full-amplitude differs notably from a linear relation. Giant spots lead to overall larger variability full-amplitudes than solar-like spots do for the same spot covering fraction. With the exception of variability full-amplitudes $\leq 1\%$ caused by giant spots, the linear relation is a poor approximation to the actual variability relation and underestimates the spot covering fraction. Instead, the variability full-amplitude grows asymptotically as a function of spot covering fraction.

The shaded regions in Figure 4 illustrate the dispersion in the model outcomes. In effect, a given observed variability full-amplitude corresponds to a range of spot covering fractions, which widens further for larger variability full-amplitudes. Additionally, the solar-like spots case allows for still wider ranges of spot covering fractions. Table 3 provides the values of $f_{spot,min}$, $f_{spot,mean}$, and $f_{spot,max}$ (see Section 2.2) resulting from the set of 100 variability models we conducted for each spectral type.

Following the apparent square root dependence of the variability full-amplitude A on the spot covering fraction, we fit via least squares a scaling relation of the form

$$A = C \times f_{spot}^{0.5} \quad (4)$$

to each set of models, in which C is a scaling coefficient that depends on both the spot contrast and size. We find the relationship is approximated well by Equation 4 for all spots-only models. In Table 3, we provide the fitted

values of C with an uncertainty determined by the 68% dispersion in model outcomes (i.e., the shaded regions in Figure 4).

Figure 5 shows the results of the variability modeling for the spots-and-faculae case. In contrast to the spots-only case, the addition of faculae leads to larger I-band variability full-amplitudes and a plateau in the relation for small spot covering fractions. As a result, a larger range of f_{spot} corresponds to $A = 0.01$ than in the spots-only case. Variability full-amplitudes begin to grow asymptotically again for $f_{spot} > 0.1$ because the photospheres are nearly fully covered with faculae (due to the 10:1 faculae:spot ratio) and additional faculae do not contribute to the photospheric heterogeneity. Table 4 provides the range of f_{spot} and f_{fac} in the spots and faculae case for each spectral type.

For both spots-only and spots-and-faculae models, the variability modeling results show that extrapolations assuming a linear relation between the observed variability and spot covering fraction tend to underestimate the true spot covering fraction. Additionally, there is not a one-to-one relation between the observed variability and the spot covering fraction; instead, each observed variability full-amplitude corresponds to a range of covering fractions.

3.2. Stellar contamination spectra

Figure 6 shows the contamination spectra produced by the spots-only models for three representative spectral types. The shaded regions illustrate the range of contamination spectra possible due to the range of spot covering fractions allowed. Unocculted spots lead to an increase in transit depths across the full wavelength range studied, with the largest increases at the shortest wavelengths. Variations in transit depth due to differences in the molecular opacities between the photosphere and spots are also apparent. They are strongest for mid-M dwarfs and overlap with many regions of interest for exoplanetary transmission features. We find that while the spectral type determines the specific features present, the overall scale of the contamination spectrum is largely independent of spectral type.

Spot size, however, has a strong effect on the scale of the contamination spectra for a given covering fraction. Considering the mean spot covering fractions consistent with a 1% variability full-amplitude, giant spots alter transit depths by an average of 0.4% across 0.3–5.5 μm wavelengths for M dwarf spectral types. Given the allowed range of spot covering fractions, however, the average change could be as low as 0.2% or as high as 0.9%. Solar-like spots, by contrast, produce much larger changes to transit depths due to the larger spot

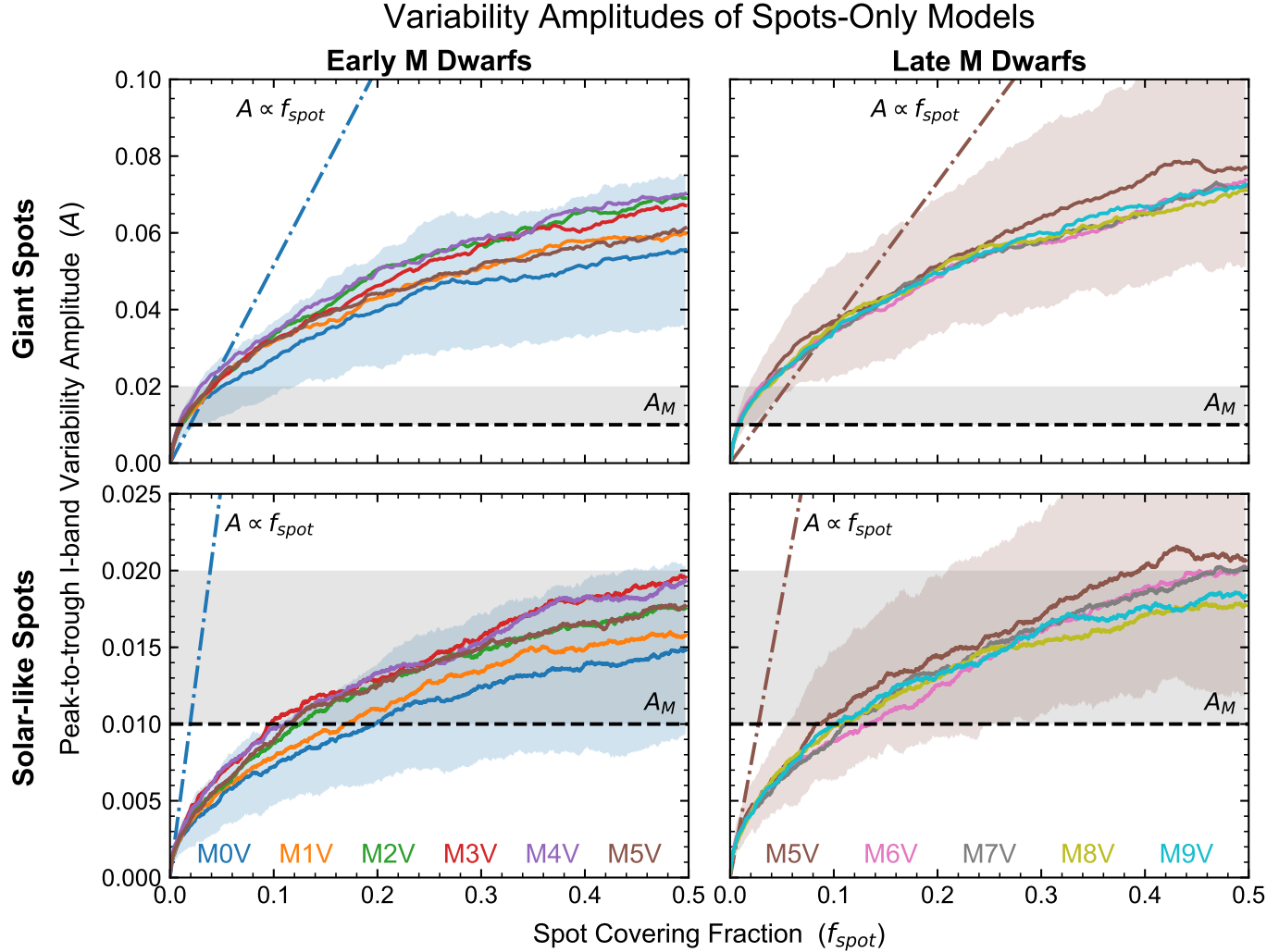


Figure 4. Variability full-amplitudes as a function of spot covering fraction for the spots-only case. Results from PHOENIX and DRIFT-PHOENIX models are shown in the left and right columns, respectively. Results using giant and solar-like spots are shown in the top and bottom rows, respectively. Note the difference in vertical scale in the upper and lower panels. Solid lines give the mean spot covering fraction for each spectral type and the shaded region indicates the range encompassing 68% of the model outcomes for the earliest spectral type in each plot, which is comparable to the dispersion in model outcomes for all other spectral types. Additionally, the expected relation if variability were a linear function of spot covering fraction is shown as a dash-dotted line, given the I-band photosphere and spot fluxes of the earliest spectral type. The horizontal dashed lines show the TRAPPIST-1 variability full amplitude and the gray shaded region highlights the range of typical M dwarf photometric modulations detected by [Newton et al. \(2016\)](#). For each case, the variability grows asymptotically as a function of f_{spot} and the linear relation generally underestimates f_{spot} . The dispersion in model outcomes demonstrates that a range of spot covering fractions corresponds to a given variability.

covering fractions present in this case. In this case, the average change to transit depths at these wavelengths for the mean spot covering fraction is 5.0% and could be as low as 2.6% or as high as 16%, considering the allowed range of spot covering fractions.

Figure 7 shows contamination spectra produced by the spots and faculae variability models. In the giant spots case, the contamination spectra for all M dwarf spectral types are dominated in the 0.3–5.5 μ m wavelength range by the facular contribution, which reduces transit depths at these wavelengths. Comparing Tables 3 and

4 shows that spot filling factors in all giant spots cases are very low, typically $\lesssim 1\%$, but they are on average 2.2 \times smaller in the giant spots and faculae case than in the giant spots-only case. Thus, a general finding is that the facular component can dominate the visual and near-infrared contamination spectra for low spot covering fractions. On average, in the giant spots and faculae case, transit depths are decreased by 0.4% across this wavelength range for M dwarf spectral types. Given the range of allowed spot- and faculae-covering fractions in these models, this average decrease could be as low as

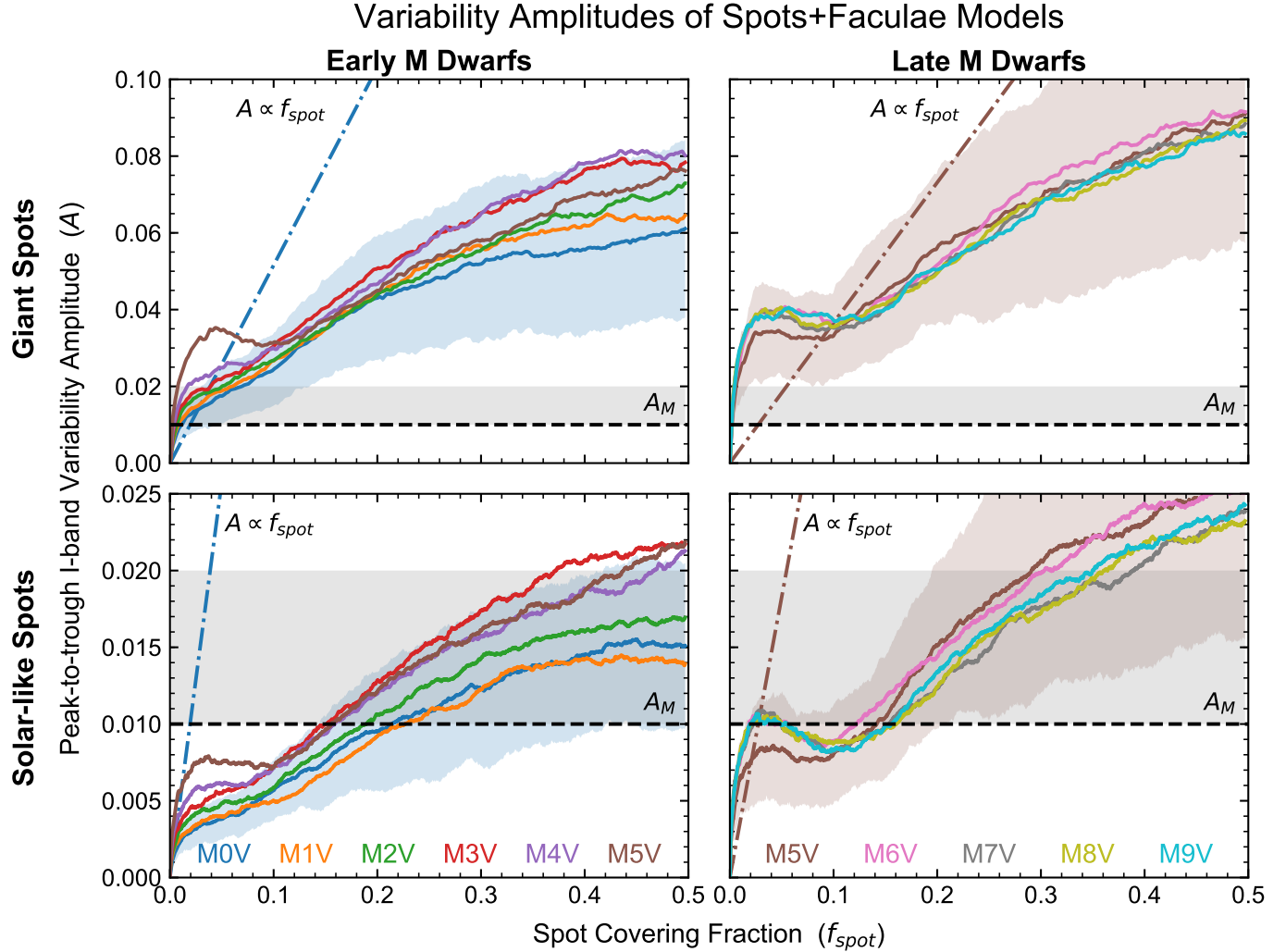


Figure 5. Variability full-amplitudes as a function of spot covering fraction for the spot-and-faculae case. Note the difference in vertical scale in the upper and lower panels. Figure elements are the same as those in Fig. 4. In contrast to the spots-only case, the addition of faculae in the variability modeling leads to larger variability amplitudes and a relative plateau in the relation for spot covering fractions $f_{spot} < 0.1$.

0.3% or high as 0.9%. However, the contamination spectra of all M dwarf spectral types are more pronounced at shorter wavelengths, producing a mean decrease in transit depth of 2.4% for 0.3–1 μm wavelengths. We note this result is consistent with the visual transmission spectrum of GJ 1214b (Rackham et al. 2017), which orbits a mid-M dwarf host star.

The case of solar-like spots and faculae presents a challenge to our original assumption of an immaculate transit chord. The facular coverages determined in these models are typically $> 50\%$ and range as high as 72%. If these facular coverages were indeed present, faculae would represent the dominant component of the stellar disk and likely the transit chord as well, precluding attempts to mask faculae crossings in light curves. Therefore, we assume in this case that the the faculae-covering fraction within the transit chord is roughly equivalent

to that of the unocculted stellar disk and we calculate the contamination spectra shown in Figure 7 without the contribution from a faculae heterogeneity. Nonetheless, the range of facular-covering fractions presented in Table 4, particularly for late M dwarfs, shows that facular coverages are largely unconstrained and thus a wide range of facular contributions to stellar contamination spectra are possible for the solar-like spots case.

Regardless of the precise contribution from faculae, the addition of faculae to the heterogeneity model for the solar-like spots case generally increases the spot covering fractions that are consistent with an I-band variability full-amplitude of 1% (Table 4). On average, spot covering fractions in the solar-like spots and faculae case are $1.2 \times$ larger than those in the case of solar-like spots only, leading to an average increase in transit depth across M

Table 4. Filling factors determined by spots and faculae models

Sp. Type	Model Grid	$f_{spot,min}$	$f_{spot,mean}$	$f_{spot,max}$	$f_{fac,min}$	$f_{fac,mean}$	$f_{fac,max}$
Giant Spots and Faculae							
M0V	PHOENIX	0.006	0.011	0.044	0.058	0.106	0.367
M1V	PHOENIX	0.005	0.008	0.029	0.047	0.082	0.265
M2V	PHOENIX	0.004	0.007	0.019	0.039	0.066	0.183
M3V	PHOENIX	0.003	0.005	0.016	0.032	0.049	0.158
M4V	PHOENIX	0.003	0.004	0.009	0.029	0.042	0.096
M5V	PHOENIX	0.003	0.003	0.005	0.024	0.030	0.051
M5V	DRIFT-PHOENIX	0.003	0.003	0.004	0.023	0.029	0.046
M6V	DRIFT-PHOENIX	0.003	0.003	0.004	0.023	0.025	0.040
M7V	DRIFT-PHOENIX	0.003	0.003	0.004	0.023	0.025	0.038
M8V	DRIFT-PHOENIX	0.003	0.003	0.003	0.024	0.025	0.035
M9V	DRIFT-PHOENIX	0.003	0.003	0.003	0.024	0.026	0.037
Solar-like Spots and Faculae							
M0V	PHOENIX	0.14	0.21	0.44	0.68	0.72	0.56
M1V	PHOENIX	0.16	0.23	0.34	0.69	0.72	0.65
M2V	PHOENIX	0.12	0.19	0.38	0.65	0.72	0.62
M3V	PHOENIX	0.10	0.15	0.26	0.58	0.69	0.71
M4V	PHOENIX	0.11	0.16	0.32	0.62	0.70	0.67
M5V	PHOENIX	0.06	0.16	0.33	0.45	0.70	0.66
M5V	DRIFT-PHOENIX	0.02	0.14	0.21	0.15	0.68	0.72
M6V	DRIFT-PHOENIX	0.01	0.06	0.25	0.09	0.44	0.71
M7V	DRIFT-PHOENIX	0.01	0.10	0.26	0.08	0.60	0.71
M8V	DRIFT-PHOENIX	0.01	0.10	0.26	0.08	0.58	0.71
M9V	DRIFT-PHOENIX	0.01	0.05	0.24	0.08	0.39	0.72

NOTE—Section 2.2 provides the definitions of the spot covering fractions $f_{spot,min}$, $f_{spot,mean}$, and $f_{spot,max}$, and the faculae covering fractions $f_{fac,min}$, $f_{fac,mean}$, and $f_{fac,max}$.

dwarf spectral types of 5.8% in the 0.3–5.5 μm wavelength range.

4. DISCUSSION

We find that, for a range of host star spectral types, heterogeneous stellar photospheres strongly alter transmission spectra. In the following sections, we compare the spot and faculae covering fractions determined by our modeling efforts with empirical results, discuss the effect of stellar contamination on derived planetary parameters, and examine the example of the TRAPPIST-1 system in detail.

4.1. Comparison with empirical results

Active region properties such as fractional areal coverage are difficult to ascertain in spatially unresolved observations of stars. However, estimates can be made based on the unique properties of chromospheric line

formation in the specific case of M dwarf stars. In brief summary, the H α line appears only weakly in absorption in the cool photospheres of M dwarfs. However, as demonstrated by Cram & Mullan (1979), the onset of chromospheric heating leads first to an increase in absorption strength of the line. With further non-radiative heating the line eventually attains a maximum in absorption equivalent width. Enhanced heating causes H α to become collisionally controlled and driven into emission as the defining observational characteristic of a dMe star.

Based on this general behavior of H α line formation in M dwarfs, Giampapa (1985) discussed how the observed equivalent width of H α absorption yields estimates of the *minimum* area coverage of active regions. Since it is a chromospheric feature, its observed strength will be a function of its intrinsic absorption in plage and the

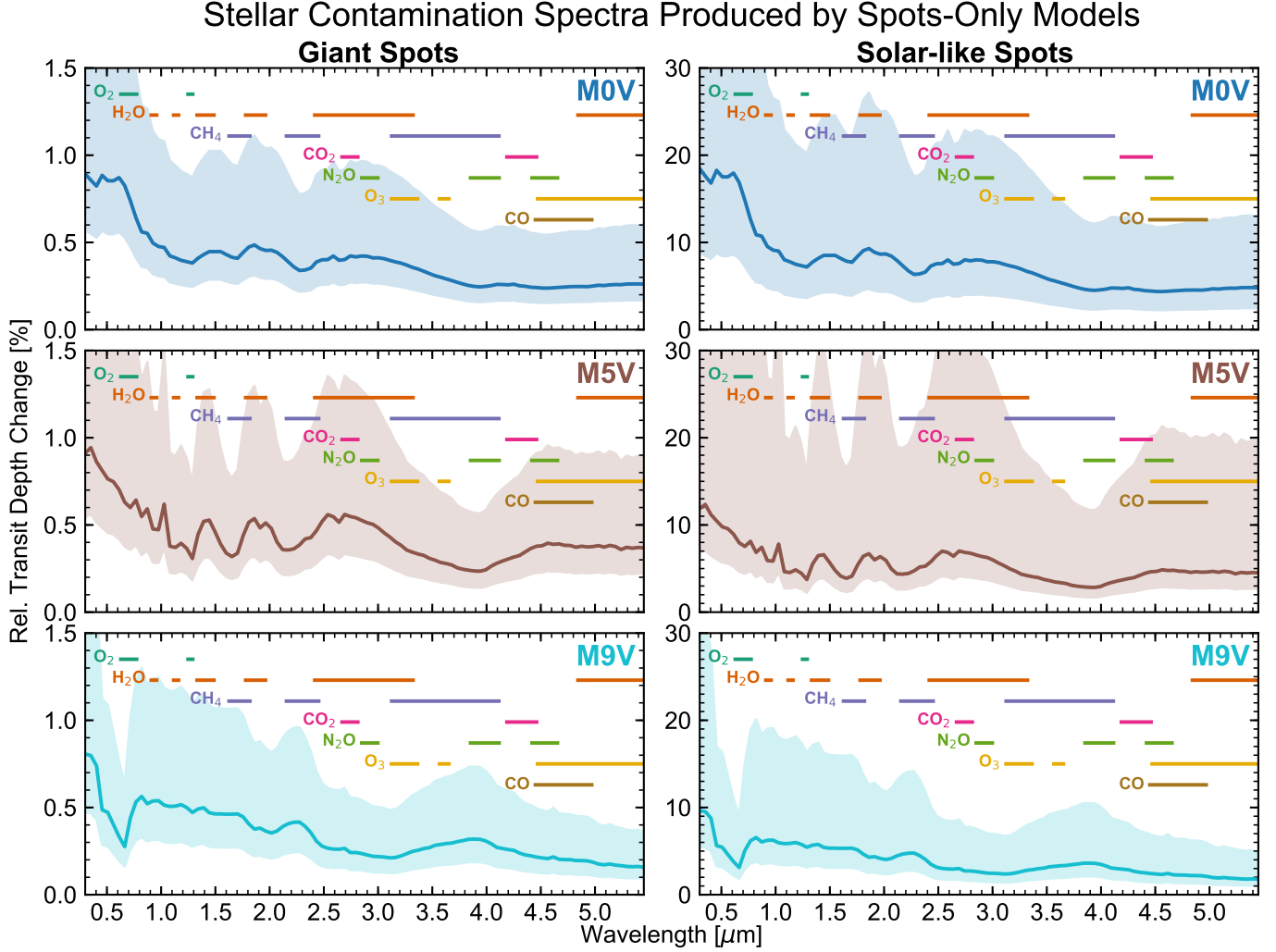


Figure 6. Stellar contamination spectra produced by spots-only models. Contamination spectra for early, mid, and late M dwarf spectral types are shown. Models for giant (solar-like) spots are shown in the left (right) column. Solid lines give the contamination spectrum for the mean spot covering fraction consistent with a 1% variability full-amplitude. The shaded regions illustrate the range of contamination spectra produced by spot covering fractions consistent with that same variability (see Table 3). Overlapping wavelength bands for key exoplanetary atmospheric features are given.

total fractional area coverage of associated magnetically active facular regions. For specific M dwarf (non-dMe) stars with measurements available at that time, ranging in spectral type from M1.5 to M5.5, he deduced model-independent filling factors of facular regions exceeding 10–26%. A more stringent inference of minimum filling factor can be obtained from calculations of the maximum H α absorption equivalent width attained in M dwarf model chromospheres. Based on these computations (Cram & Mullan 1979), Giampapa (1985) found a range in the minimum active region filling factor of 31–67% in the case of non-dMe stars characterized by $(R - I)_K = 0.9$, corresponding to about $T_{eff} = 3500$ K. Therefore, the fractional area coverage of faculae of even relatively quiescent M dwarfs is widespread.

In the case of dMe stars, more intense chromospheric heating gives rise to H α emission which by itself does not lead to a direct estimate of facular area coverage. However, there is direct observational evidence for widespread, multi-kilogauss magnetic fields outside of spots in active M dwarfs (i.e., dMe stars) at high filling factors in excess of 50% based on the analysis of magnetically sensitive photospheric features (Saar & Linsky 1985; Reiners et al. 2009). Furthermore, the absence of any reported rotational modulation of H α emission in dMe stars is consistent with the occurrence of an azimuthally symmetric, spatially widespread presence of facular regions on their surfaces.

In addition to active regions characterized by bright chromospheric emission or, in the case of quiescent M dwarfs, chromospheric H α absorption, the occurrence

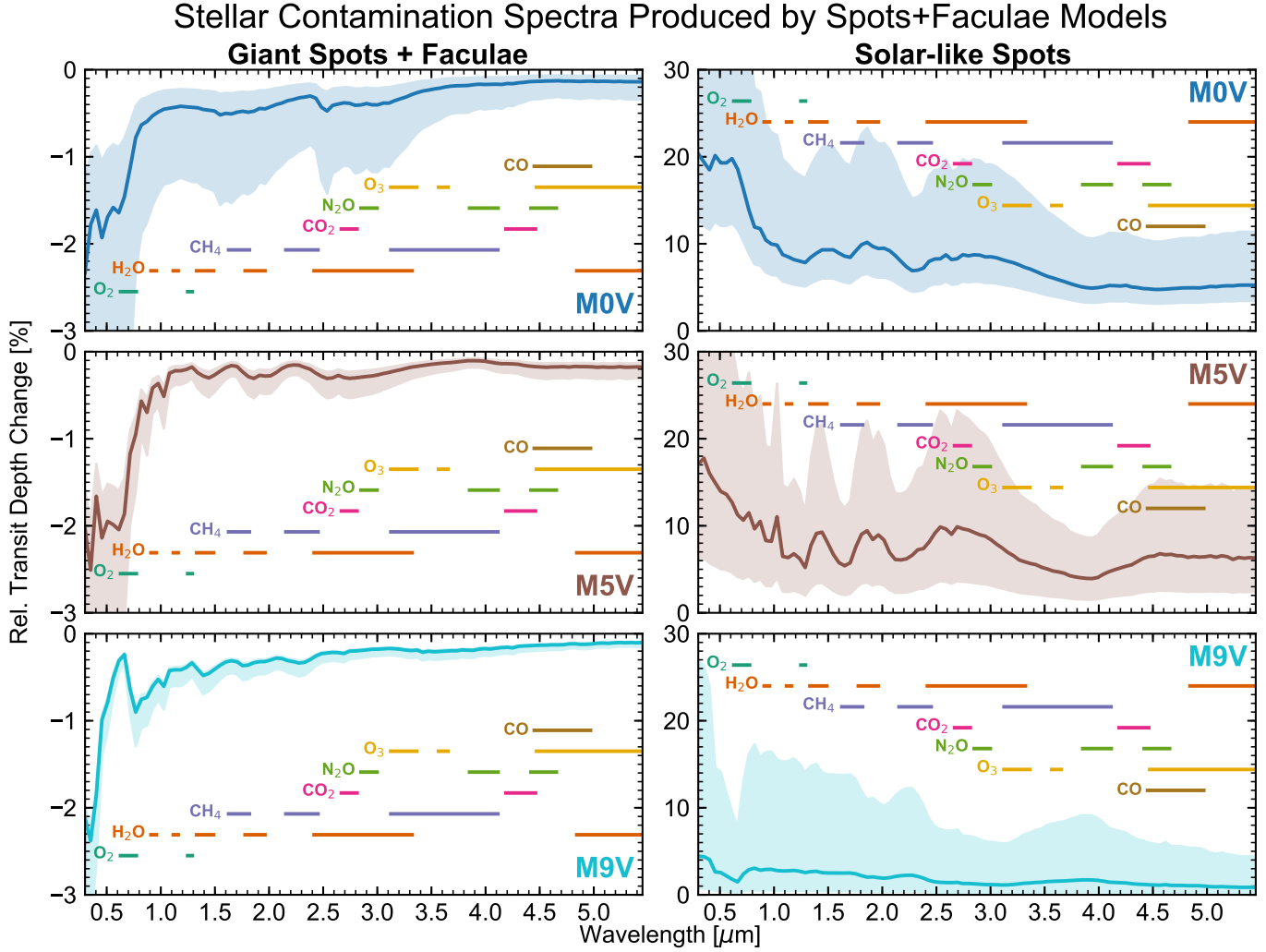


Figure 7. Stellar contamination spectra produced by spots and faculae models. The figure elements are the same as those in Figure 6.

of periodic or quasi-periodic light curve modulations in photometric bandpasses, indicative of the presence of cool spots, has an extensive record of observations. In a study of a compilation of extensive datasets, [Newton et al. \(2016, 2017\)](#) measured photometric semi-amplitudes in the range of roughly 0.5–4% ([Newton et al. 2017](#), Fig. 9). We can therefore infer minimum starspot filling factors $f_{\text{spot}} \sim 1\text{--}8\%$ of the visible stellar disk in the case of completely black spots. Estimates of starspot temperatures provide a further refinement of the minimum spot filling factor. In an investigation of the magnetic properties of spots on the active, early M dwarf AU Mic (dM1e), [Berdyugina \(2011\)](#) utilized polarimetric observations of temperature- and magnetically-sensitive diatomic molecules to find spot temperatures $\sim 500\text{--}700$ K cooler than the surrounding photosphere, and with associated magnetic field strengths as high as 5.3 kG. With an effective temperature of 3775 K ([Pagano et al. 2000](#)), the ratio of

spot-to-stellar effective temperature is in the range of 0.81–0.87. In general, [Afram & Berdyugina \(2015\)](#) find for M dwarfs that spot models tend to have a spot-to-photosphere temperature ratio of 0.86. Based on these measurements, for a semi-amplitude of $\sim 2\%$ with a range of $T_{\text{spot}}/T_{\text{eff}}$ of ~ 0.8 to 0.9 we estimate spot filling factors in the range of $\sim 7\text{--}12\%$. Given that the photometric modulation depends on both contrast and departures from a longitudinally symmetric surface distribution of spots, this spot filling factor estimate should be regarded as a minimum value since the observed light curve modulation could arise from departures from axial symmetry in an otherwise widespread and uniform distribution of small spots. In fact, [Jackson & Jeffries \(2013\)](#) demonstrate that small-amplitude light curve modulation can arise from the combined effect of a random distribution of small spots characterized by a uniform size (i.e., scale length) and a plausible temperature contrast with the surrounding photosphere of

0.7. As an illustration, their Monte Carlo simulations of light-curve amplitudes due to a large number of randomly distributed spots with, say, a characteristic length scale of 3.5 degrees yield a mean amplitude of 1% with a filling factor of $\sim 30\%$ (Jackson & Jeffries 2013, Fig. 4) in qualitative agreement with our variability modeling. Thus, in this context, we conclude that high filling factors of spots and faculae, such as those determined in this work, are a plausible interpretation of the observed light curve modulations seen in M dwarfs.

4.2. Stellar contamination mimicking and masking exoplanetary features

As shown in Figures 6 and 7, stellar heterogeneity can introduce significant spectral features in visual and near-infrared transmission spectra. These deviations result from a difference in flux between the immaculate photosphere and heterogeneities such as spots and faculae (Equation 3). Unocculted spots introduce positive features in transmission spectra that may be mistaken for evidence of absorption or scattering in the exoplanet atmosphere. By contrast, unocculted faculae introduce negative features, which can mask genuine spectral features originating in the exoplanet atmosphere.

Figure 8 illustrates the effect of stellar contamination at visual and near-infrared wavelengths of interest for molecular features in exoplanetary atmospheres. In general, stellar contamination increases transit depths and may mimic exoplanetary features, with the exception in the case of giant spots and faculae, in which the contribution from faculae dominates and may mask exoplanetary features. Transit depth changes are largest and therefore most problematic for: 1) solar-like spots cases, 2) earlier spectral types, and 3) molecules with absorption bands at relatively short wavelengths, such as O_2 .

As a comparison for scale, the dashed horizontal line in Figure 8 indicates the 1.3% change in transit depth expected for a transiting Earth-twin (atmospheric mean molecular weight $\mu = 28.97$ amu; equilibrium temperature $T_{eq} = 288$ K) due to an atmospheric feature covering five pressure scale heights. In the giant spots cases, stellar contamination can alter transit depths at overlapping wavelengths by a non-negligible fraction of this amount, the effect of which is to boost the apparent size of features in the spots-only case and to weaken them in the giant spots and faculae case. Therefore, large unocculted spots can lead to a range of erroneous interpretations of transmission spectra: molecular abundances may appear enhanced or depleted and the presence of a obscuring haze layer can be masked or mimicked.

By contrast, solar-like spots cases increase transit depths by much more than an expected exoplanetary

feature. For early spectral types, the increase in transit depth can be more than *ten times* that expected for planetary features. Such a strong feature could be easily identified as stellar in origin, though the scale of the feature, combined with the wide range of stellar contributions possible, would limit the accuracy of any determination of the underlying planetary feature. Later spectral types present a more pathological circumstance, as the magnitude of the transit depth change due to stellar contamination is comparable to that of a planetary atmospheric feature, allowing the signals to be easily mistaken. Therefore, constraining spot sizes and, by extension, spot covering fractions, will be essential for investigations of atmospheric features in transmission spectra of low-mass exoplanets around late M dwarfs, such as the TRAPPIST-1 system. We consider this topic in more detail in Section 4.5 below.

4.3. Comparison to observational precisions

Thus far we have discussed the effect of stellar heterogeneity on transmission spectra in terms of relative transit depth changes. This approach is useful because the multiplicative change in transit depth produced by unocculted spots and faculae can be applied to any planetary transmission spectrum. However, it is also informative to convert these relative transit depth changes to absolute ones that can be compared to observational precisions afforded by current and near-future facilities.

To do this, we must adopt parameters for the transiting exoplanet. At a minimum, these are the planetary radius and the expected scale of a planetary atmospheric feature. We consider two end-member cases for this comparison: a hot Neptune and an Earth-twin. For the hot Neptune case, we adopt the parameters of GJ 436b (Butler et al. 2004; Gillon et al. 2007), which is one of the largest and hottest planets known to transit an M dwarf and represents a more readily observable exoplanet atmosphere. Its near-infrared transmission spectrum (Knutson et al. 2014) displays a weighted mean transit depth of $\bar{D} = 0.70\%$ and a 200-ppm variation in transit depth (Knutson et al. 2014), which has been interpreted as an H_2O absorption feature covering 0.46 ± 0.25 atmospheric scale heights (Crossfield & Kreidberg 2017). This feature produces a relative transit depth change of

$$\epsilon_p = \frac{\Delta D}{D} = \frac{2.0 \times 10^{-4}}{7.0 \times 10^{-3}} = 2.9\%. \quad (5)$$

We adopt this observed relative transit depth change and the best-fit planetary radius of GJ 436b ($R_p = 3.95 R_{\oplus}$; Gillon et al. 2007) for the hot Neptune case. The other end-member case we consider is that of a

Effect of Stellar Contamination on Planetary Absorption Features

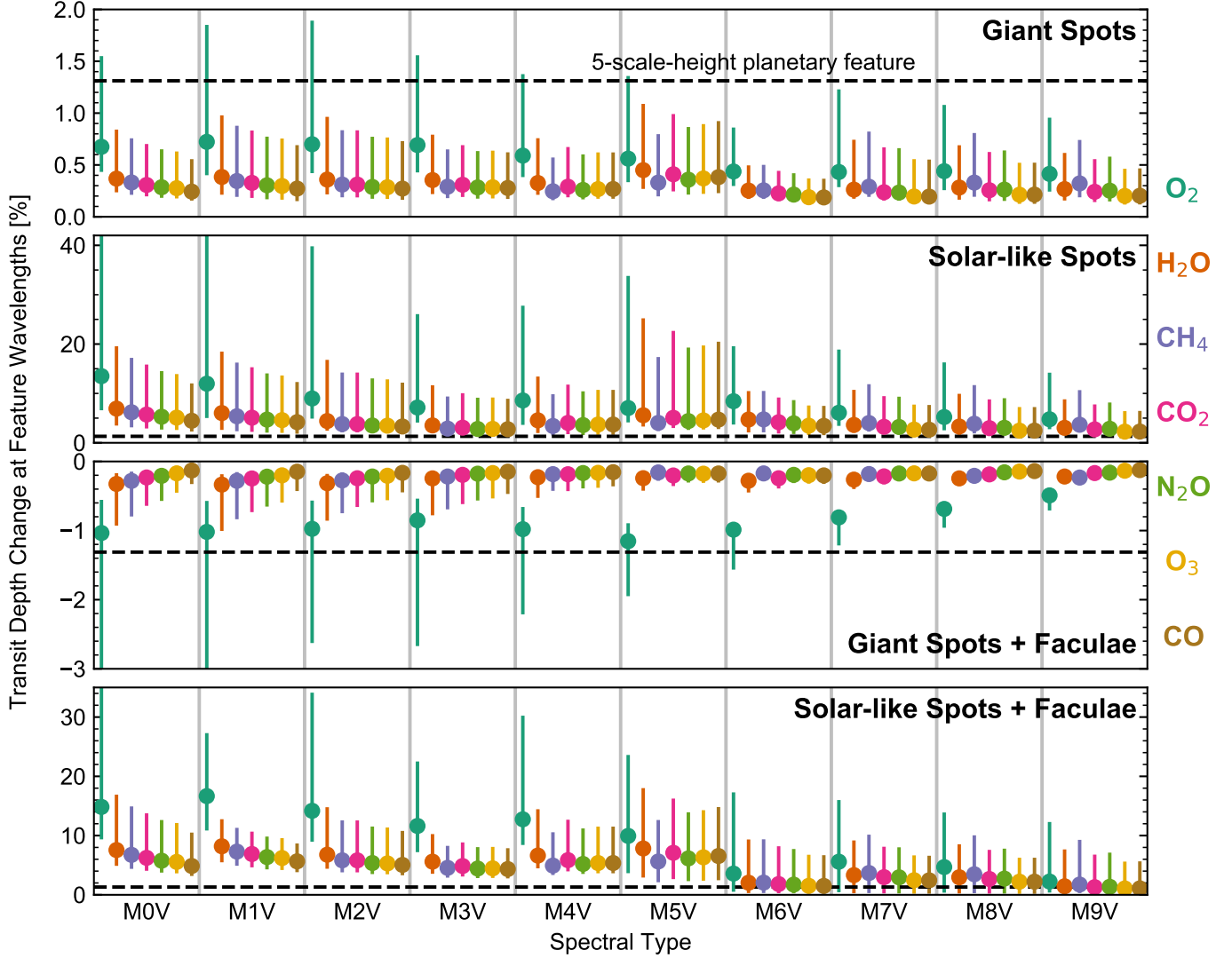


Figure 8. Effect of stellar contamination at wavelengths of planetary absorption features. The change in transit depth integrated over wavelengths of interest for molecular species is shown as a function of spectral type. From top to bottom, the panels illustrate results for four cases: giant spots, solar-like spots, giant spots and faculae, and solar-like spots and faculae. Points correspond to the mean stellar contamination signal and error bars to the dispersion in the strength of the signal illustrated by the shaded regions in Figures 6 and 7. Horizontal dashed lines show the expected transit depth change for a feature covering five scale heights in an Earth-like atmosphere, which is independent of stellar spectral type.

transiting Earth-twin ($R_p = 1.0 R_\oplus$; $\mu = 28.97$ amu; $T_{eq} = 288$ K), which produces a relative transit depth change of $\epsilon_p = 1.3\%$ for a 5-scale-height planetary feature and represents a larger observational challenge.

For each of these planetary cases, we calculate transit depths D and absolute transit depth changes due to planetary atmospheric features ΔD_p as a function of M dwarf spectral type using the stellar radii provided in Table 1. We also calculate the mean absolute transit depth change due to stellar heterogeneity ΔD_s at wavelengths of interest for H_2O absorption (as discussed in Section 4.2) for each of the four heterogeneity cases we

consider. The results are summarized in Tables 5 and 6 for the hot Neptune and Earth-twin cases, respectively. Comparing these values of ΔD_p and ΔD_s suggests that for hot Neptunes variations in transit depth due to the planetary atmosphere are roughly an order of magnitude larger than those due to stellar heterogeneity for giant spot cases. However, stellar signals are larger than planetary signals for all solar-like spot cases, with the largest difference between the signals for earlier spectral types. For Earth-twins transiting M dwarfs, in the case of giant spots, planetary signals are at least three times larger than stellar ones for all M dwarf spectral types. How-

ever, as with the hot Neptune case, stellar signals due to solar-like spots are larger than planetary signals for all M dwarf spectral types.

The question remains, however, of how these planetary and stellar signals compare to observational precisions. The most precise transmission spectrum obtained with *HST/WFC3* to date contains a typical uncertainty of 30 ppm on the transit depth in each wavelength channel (Kreidberg et al. 2014). This is similar to the noise floors for James Webb Space Telescope (*JWST*) instruments adopted by Greene et al. (2016) for wavelength ranges of interest in this study: 20 ppm for NIRISS SOSS ($\lambda = 1\text{--}2.5\ \mu\text{m}$) and 30 ppm for NIRCam grism ($\lambda = 2.5\text{--}5.0\ \mu\text{m}$). We adopt 30 ppm as a fiducial noise floor for both *HST* and *JWST* observations. Considering this detection threshold, our results suggest that planetary atmospheric features are detectable for hot Neptunes orbiting M dwarfs of all spectral types (Table 5). The effects of unocculted giant spots and facular regions are detectable for host stars with spectral types of roughly M3V and later, while in the more problematic case of solar-like spots, the effects of unocculted spots and faculae are detectable for all M dwarf spectral types. In the case of a transiting Earth-twin (Table 6), we estimate that planetary atmosphere features are detectable for spectral types M6V and later. The effects of unocculted giant spots and facular regions may alter the strength of these features by $\sim 20\%$ but will only independently reach the detection threshold of 30 ppm for M9V host stars. However, in the case of solar-like spots, we estimate that the effects of unocculted spots and faculae may be apparent in observations of spectral types as early as M3V or M4V.

In summary, we find that the most precise existing *HST/WFC3* G141 transmission spectra as well as upcoming *JWST* transmission spectra of small planets around M dwarfs can be significantly influenced by stellar contamination; any analysis of such spectra should consider the possible range of systematic contamination due to the transit light source effect.

4.4. Systematic errors in density measurements

As the fundamental effect of starspots in this context is to influence the apparent radius of the planet relative that of its star, we also explore here the impact of starspots on planet density measurements. Transiting planet surveys utilize visual and near-infrared bandpasses for discovery efforts (e.g., Nutzman & Charbonneau 2008; Jehin et al. 2011; Gillon et al. 2011). With the exception of *Kepler*, which utilizes a broad, unfiltered visual bandpass, these surveys typically favor redder wavelengths such as I-band in order to minimize the

contribution of stellar variability to measurements. The bulk density of an exoplanet calculated from discovery transits can provide a clue as to their volatile content, making it one of the primary factors affecting whether a planet is selected for follow-up observations. Furthermore, the unfiltered *Kepler* photometry often remains the most precise transit depth measurement for most small planets, and therefore its accuracy affects inferences made about individual planets as well as ensembles of planets.

Our work here, however, shows that the stellar contributions can be larger than previously suspected and may still contribute significantly even at red visual and near-infrared wavelengths, given the large range of stellar heterogeneity levels that may correspond to an observed rotational variability level. To determine the scale of the contribution, we calculated the range of radius and, by extension, density errors by integrating the contamination spectra presented in Section 3.2 over the Bessel I-band filter bandpass, which is similar to bandpasses used by ground-based transit surveys such as MEarth (Nutzman & Charbonneau 2008) and TRAPPIST (Gillon et al. 2011; Jehin et al. 2011), and the *Kepler*³ and *TESS* (Ricker et al. 2015; Sullivan et al. 2015) spectral responses.

The resulting systematic radius and density errors are shown in Figure 9. Positive radius errors, which indicate the apparent planetary radius is larger than the true planetary radius, correspond to negative density errors, which indicate that the apparent density is smaller than the true bulk density. We note that this systematic density error provides only a minimum estimate of the total error in planetary bulk density, to which the observational uncertainty in radius and any error in mass estimate must be also be added.

As with the investigation into false planetary absorption features, we find the primary determinant of the systematic density error to be the spot size. Small spots cases are the most problematic, with an average density error of 13% across all spectral types and bandpasses that we considered and a maximum of 29% for M1 dwarfs in the *Kepler* bandpass. In the giant spots cases, by contrast, density errors are 1% on average and the largest are 3%. Aside from spot size, spectral type is the second-largest determinant of the systematic error. Earlier M dwarf spectral types tend to produce density errors that are larger on average. Additionally, they demonstrate a larger dispersion in possible errors, as indicated by the error bars, given the wider range of

³ <https://archive.stsci.edu/kepler/fpc.html>

Table 5. Transit depths and absolute transit depth changes for a representative hot Neptune by spectral type

Sp. Type	D	ΔD_p	ΔD_s by Heterogeneity Case			
			Giant Spots		Solar-like Spots	Giant Spots + Faculae
			(ppm)	(ppm)	(ppm)	(ppm)
M0V	3400	99	13	240	-11	260
M1V	5400	160	21	330	-18	450
M2V	6800	200	24	300	-21	460
M3V	8600	250	30	300	-21	480
M4V	19000	560	63	880	-44	1300
M5V	33000	950	100	1100	-85	1900
M6V	58000	1700	150	2700	-160	1200
M7V	91000	2600	240	3300	-240	3000
M8V	110000	3100	300	3600	-260	3200
M9V	200000	5900	550	6200	-450	2900

NOTE—Listed are the planetary transit depth D , transit depth change due to planetary atmospheric features ΔD_p , and, for the four heterogeneity cases we consider, the transit depth change due to stellar heterogeneity ΔD_s (shown in bold for cases in which the stellar transit depth change is larger than that due to planetary atmospheric features). The scale of the stellar signal is smaller than that of a hot Neptune atmospheric feature for all giant spots cases, but it is generally larger than the planetary signal for cases with solar-like spots.

spot and faculae covering fractions corresponding to an observed variability (see Tables 3 and 4). Finally, we find that the systematic errors are generally larger for bluer observational bandpasses, though the effect of the bandpass is smaller than that of either the spot size or host star spectral type.

To place the systematic radius errors in context, the difference in radius between an entirely rocky composition and a planet with 25% H_2O by mass for planets with masses between 0.125 and 32 Earth masses is 10–12% (Zeng et al. 2016, Table 2), illustrated by the shaded regions in Figure 9. In terms of an observational comparison, we note that the 1-sigma uncertainty on the radius of LHS 1140b is 7.0% (Dittmann et al. 2017), giving it one of the best constrained densities of a sub-Neptune exoplanet to date. Therefore, while the effect of unocculted giant spots is easily hidden within observational uncertainties, unocculted solar-like spots can introduce a systematic error in radius that is comparable to the total error combined from the observational uncertainties in the radial velocity and transit photometry measurements and can significantly alter interpretations of the volatile content of an exoplanet. We note that this applies to M dwarf planets that will be discovered by TESS, for which we predict sunspot-like spots

will lead on average to systematic radii overestimates of 4.3% and density underestimates of 13%.

4.5. Application to TRAPPIST-1 system

We utilized the approach detailed in Section 2 to place constraints on spot and faculae covering fractions for TRAPPIST-1 and their effects on observations of the TRAPPIST-1 planets. We opted to explore the case of the TRAPPIST-1 planets because currently they represent the best examples of habitable zone, possibly rocky planets and these planets are also likely to be primary targets for in-depth *JWST* transit spectroscopy.

4.5.1. Spot and faculae covering fractions

We adopted the stellar parameters for TRAPPIST-1 from Gillon et al. (2017), including stellar mass, radius, effective temperature, and metallicity. With these parameters, we interpolated spectra covering 0.3–5.5 μm from the DRIFT-PHOENIX model grid. We set the photosphere temperature to the effective temperature and calculated the spot and faculae temperatures using the relations outlined in Section 2.1.

We integrated these spectra over the Bessel I-band response, similar to the I+z bandpass utilized by the TRAPPIST survey (Gillon et al. 2016, 2017), to simulate the contributions of these spectral components to

Table 6. Transit depths and absolute transit depth changes for a transiting Earth-twin by spectral type

Sp. Type	D	ΔD_p	ΔD_s by Heterogeneity Case			
			Giant Spots		Solar-like Spots	Giant Spots + Faculae
			(ppm)	(ppm)	(ppm)	(ppm)
M0V	220	2.8	0.8	15	-0.7	16
M1V	350	4.5	1.3	21	-1.2	29
M2V	430	5.6	1.6	19	-1.4	29
M3V	550	7.2	2.0	19	-1.4	31
M4V	1200	16	4.0	56	-2.8	82
M5V	2100	27	6.5	73	-5.4	120
M6V	3700	48	9.4	180	-10	76
M7V	5800	76	15	210	-15	190
M8V	6900	90	20	230	-17	210
M9V	13000	170	35	400	-29	190

NOTE—Listed are the planetary transit depth D , transit depth change due planetary atmospheric features ΔD_p , and, for the four heterogeneity cases we consider, the transit depth change due to stellar heterogeneity ΔD_s (shown in bold for cases in which the stellar transit depth change is larger than that due to planetary atmospheric features). The scale of the stellar signal is smaller than that of an Earth-twin atmospheric feature for all giant spots cases, but it is larger than the planetary signal for all cases with solar-like spots.

photometric observations. From visual inspection of Extended Data Figure 5 of Gillon et al. (2016), we estimate the variability full-amplitude of TRAPPIST-1 to be 1 %.

Long-baseline monitoring of TRAPPIST-1 using the Spitzer Space Telescope, covering 35 transits, shows no definitive evidence of spot crossings (Gillon et al. 2017). Likewise, no spot crossings are apparent in existing *HST/WFC3* transit observations of TRAPPIST-1b and TRAPPIST-1c covering 1.1–1.7 μm with the G141 grism (de Wit et al. 2016), though the precision of G141 observations has allowed for the detection of large spot crossing events in other M dwarf transit observations (Kreidberg et al. 2014). Therefore, we assume that the presence of very large spots like those detected through molecular spectropolarimetry on active M dwarfs (Berdugina 2011), each covering 0.5% of the projected stellar disk and comparable in size to the TRAPPIST-1 planets, is unlikely. Accordingly, we adopt a spot size of 2° (400 ppm or 0.04% of the projected stellar disk), typical of large spot groups on the Sun (Mandal et al. 2017). Given the radius of TRAPPIST-1 ($R = 0.117 \pm 0.0036$; Gillon et al. 2017), this translates to spots with a radius of $R_{\text{spot}} = 1.63 \pm 0.50 \times 10^3$ km.

The left panel of Figure 10 displays the results of our variability modeling for both spots-only and spots and

faculae cases. For both cases, we find a large range of spot covering fractions is consistent with the observed variability full-amplitude. We find $f_{\text{spot}} = 11_{-6}^{+18}\%$ for the spots-only case, in which the quoted value is the mean spot covering fraction and the uncertainty refers to 68% dispersion in model results. For the spots and faculae case, we find $f_{\text{spot}} = 8_{-7}^{+18}\%$ and $f_{\text{fac}} = 54_{-46}^{+16}\%$. By contrast, under the assumption that the distribution of photospheric heterogeneities is fully asymmetric, in which case the variability amplitude would scale linearly with the spot covering fraction with a slope determined by the spot and photosphere I-band fluxes, one would infer a spot covering fraction of 1.0%. We conclude that spot and faculae covering fractions for TRAPPIST-1 are largely unconstrained by the observed photometric variability amplitude, though the allowed range of fractions is typically much larger than one would infer by assuming a linear relation between spot covering fraction and variability amplitude.

4.5.2. Stellar contamination in transmission spectra

The visual and near-infrared contamination spectra produced by the wide range of spots we infer for TRAPPIST-1 are shown in the center panel of Figure 10. The stellar contamination is a multiplicative effect and independent of the planetary transmission

Effect of Stellar Contamination on Planetary Density Calculation

Kepler TESS I-band

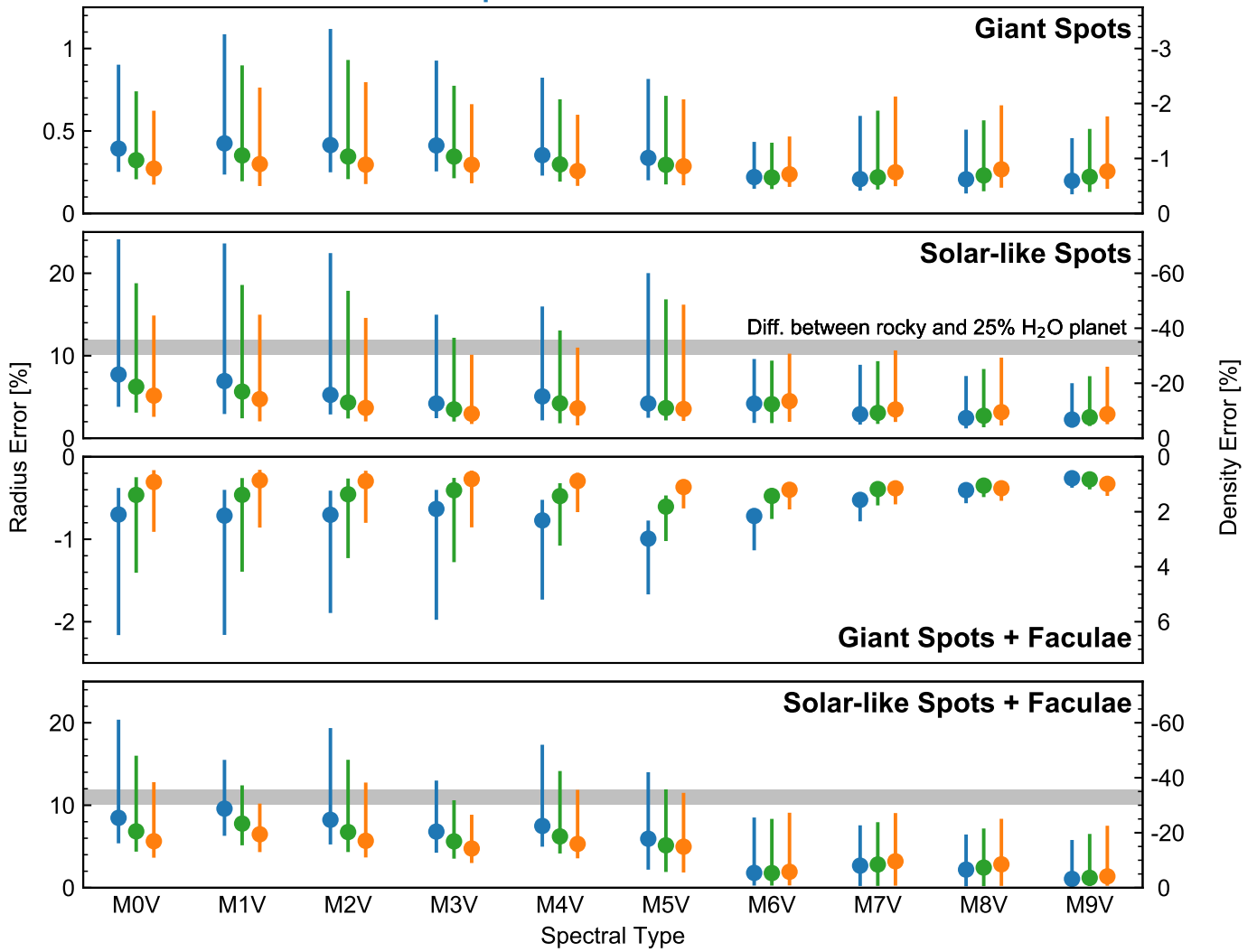


Figure 9. Effect of stellar contamination on planetary density calculation. The systematic radius error is shown as a function of spectral type. The corresponding density error is shown at right. Note the difference in sign. The panels illustrate results from four cases of heterogeneities as shown in Figure 8. Colors correspond to the *Kepler* (blue), *TESS* (green), and I-band (orange) photometric bands. The mean radius error is shown as a point and error bars correspond to the dispersion in the strength of the contamination signal (see Figures 6 and 7). The gray shaded region illustrates the relative difference in radius between an entirely rocky exoplanet and one with a significant volatile content for a range of masses between 0.125 and 32 Earth masses (see text).

spectrum (Equation 2). Thus, these relative transit depth changes are applicable to observations of each exoplanet in the TRAPPIST-1 system. As with the solar-like spot models in Figure 7, contributions from unocculted faculae are not included, given that faculae covering fractions in our models are typically $> 50\%$ and are therefore likely to be distributed homogeneously throughout the stellar disk. However, we calculate the contribution of unocculted spots using the spot covering fractions determined by the spots and faculae models, which are generally smaller than those from the spots-

only models, to exploit the increased realism of the spots and faculae models. The solid line shows the contamination spectrum corresponding to the mean spot covering fraction and the shaded region the range of spectra for the 68% confidence interval on f_{spot} . Compared to the contamination spectrum predicted by the fully asymmetric assumption, shown as a dash-dotted line, we find the level of stellar contamination to be roughly an order of magnitude larger.

Integrating over wavelengths of interest for key planetary molecular features, we illustrate the practical im-

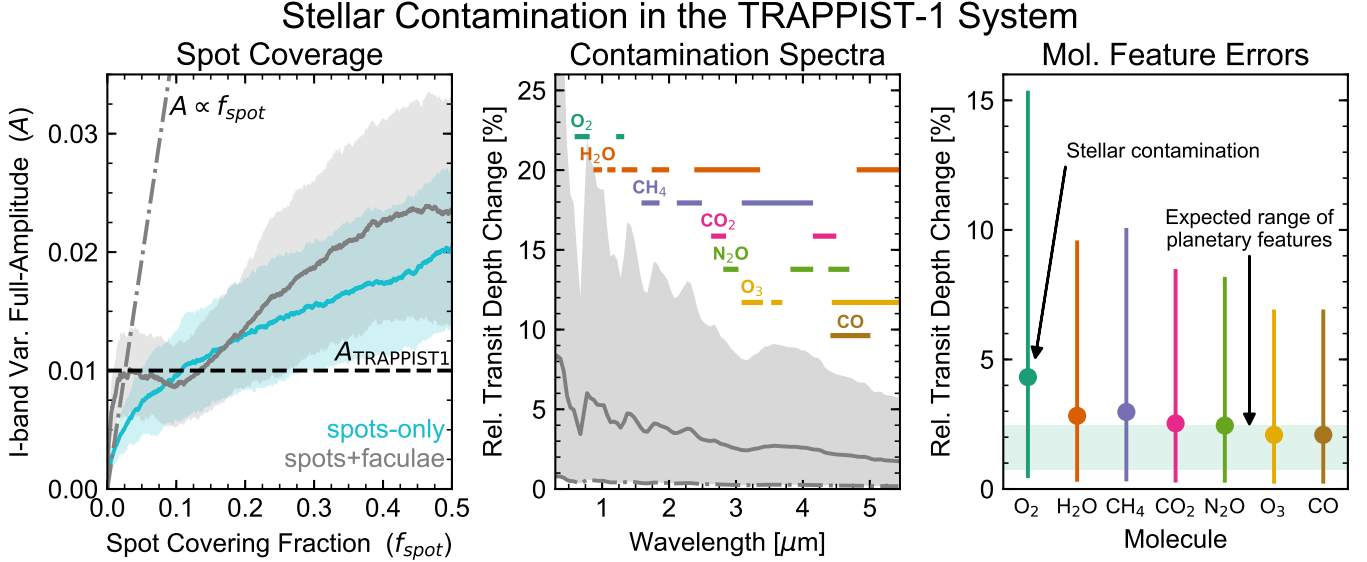


Figure 10. Summary of the effect of stellar heterogeneity in the TRAPPIST-1 system. The left panel shows I-band variability full-amplitudes as a function of spot covering fraction for spots-only (teal) and spots and faculae (gray) cases. Results from solar-like spots models are shown. The plot elements are the same as those in Figure 4. The central panel shows the contamination spectra produced by spot covering fractions consistent with the observed variability of TRAPPIST-1. The plot elements are the same as those in Figure 6. The right panel shows the relative transit depth change at wavelengths of interest for key molecular features in exoplanet atmospheres. The shaded region illustrates the range of relative transit depth changes of interest for atmospheric features from the TRAPPIST-1 planets, assuming a 5 scale height feature in an Earth-like atmosphere

pact on observations in the right panel of Figure 10. For all molecules considered, we find the mean relative transit depth change to be comparable to or larger than that produced by an exoplanetary atmospheric feature. The shaded region in this panel illustrates the range of feature scales for the six innermost TRAPPIST-1 planets, calculated using the planetary parameters from Gillon et al. (2017) and assuming an Earth-like atmospheric mean molecular weight ($\mu = 28.97$ amu). They range from 0.8% for TRAPPIST-1g to 2.5% for TRAPPIST-1d. Given the transit depths of the TRAPPIST-1 planets, these correspond to absolute transit depth changes of 59 ppm (TRAPPIST-1g) to 168 ppm (TRAPPIST-1b). Assuming the same 30 ppm detection threshold as in Section 4.3, atmospheric features with these scales are, in principle, detectable with both *HST* and *JWST*. In contrast to the planetary atmospheric signal, mean molecular feature errors produced by unocculted spots range from 2.1% for CO to 4.3% for O₂. For the planet with the shallowest transit depth in this set, TRAPPIST-1d ($D = 0.367 \pm 0.017\%$; Gillon et al. 2017), a 2.1% relative change in transit depth corresponds to an absolute transit depth change of 77 ppm, which illustrates that the range of uncertainties we predict for all molecular features for the TRAPPIST-1 planets are above the fiducial 30 ppm noise floor. In other words, we predict stellar heterogeneity will significantly impact the interpretation of high-precision TRAPPIST-1 transmis-

Table 7. Revised densities for the TRAPPIST-1 planets

Planet	Density from Gillon et al. (2017)	Revised Density	
		(ρ_{\oplus}^a)	(ρ_{\oplus})
b	0.66 ± 0.56	$0.68^{+0.67}_{-0.58}$	
c	1.17 ± 0.53	$1.21^{+0.68}_{-0.57}$	
d	0.89 ± 0.60	$0.92^{+0.73}_{-0.63}$	
e	0.80 ± 0.76	$0.83^{+0.90}_{-0.79}$	
f	0.60 ± 0.17	$0.62^{+0.23}_{-0.19}$	
g	0.94 ± 0.63	$0.97^{+0.77}_{-0.66}$	

^a $\rho_{\oplus} = 5.51 \text{ g cm}^{-3}$

NOTE—No mass and therefore density estimate for TRAPPIST-1h is available from Gillon et al. (2017).

sion spectra. Errors are most pronounced for molecules with absorption bands at shorter wavelengths. Large uncertainties exist for each molecular feature error due to the wide range of spot covering fractions and accompanying contamination spectra possible.

Finally, we calculate density errors for the TRAPPIST-1 planets due to stellar contamination. Integrating the contamination spectra presented in the center panel of Figure 10 over the Spitzer/IRAC 4.5- μm bandpass, we find an integrated systematic radius error of $\delta(R_p) = 1.1^{+2.5}_{-1.0}\%$, in which the quoted value is the mean and the error refers to the 68% dispersion in modeling results. These values translate to density errors of $\Delta(\rho) = -3^{+3}_{-8}\%$; in other words, overestimating the planetary radius leads to an underestimate of the planetary density. Such a systematic error in density measurements could lead to overestimates of the volatile content of the TRAPPIST-1 planets. We provide updated densities for the six innermost TRAPPIST-1 planets in Table 7, adjusting the values reported by Gillon et al. (2017) for the density error due to stellar contamination. Our analysis suggests that stellar contamination may be partially responsible for the relatively low densities reported for planets in this system. More generally, this effect will be an important consideration when selecting targets for characterization follow-up from among a photometrically detected sample.

5. CONCLUSIONS

We have presented an examination of stellar contamination in visual and near-infrared (0.3–5.5 μm) transmission spectra of M dwarf exoplanets using model photospheres for M0–M9 dwarf stars with increasing levels of spots and faculae. Our key findings are the following.

1. For a given spot covering fraction, larger spots will produce a larger observed variability amplitude than that of smaller spots. Constraining the typical spot size for exoplanet host stars is therefore crucial, since it will mediate the relationship between spot covering fraction and observed variability amplitude.
2. The relationship between spot covering fraction and observed variability amplitude is non-linear, scaling generally like a square root relation (Equation 4) with a coefficient $0.02 < C < 0.11$ that depends on spot contrast and size. As such, previous corrections that have assumed a linear relationship between these variables likely underestimate the true spot covering fraction and, therefore, spectral contamination due to unocculted spots. We will explore this further in an upcoming paper.
3. In contrast to the low levels of spot covering fractions ($\sim 1\%$) used in the literature, we show that a given variability amplitude corresponds to a wide range of spot and faculae covering fractions. For example, assuming spot sizes similar

to those of sunspots, we find a typical variability amplitude may correspond to spot covering fractions $0.14 > f_{spot} > 0.44$ and faculae covering fractions $0.56 > f_{fac} > 0.72$ for M0 dwarfs and $0.01 > f_{spot} > 0.24$ and $0.08 > f_{fac} > 0.72$ for M9 dwarfs. These wide ranges correspond to a similarly large uncertainty in the level of stellar contamination present in transmission spectra.

4. In stars with very large spots, the stellar contamination signal in the 0.3–5.5 μm wavelength range can be dominated by the contribution from unocculted faculae, thereby decreasing observed transit depths. However, for stars with solar-like spots and the same observed variability, we find facular coverage to be so widespread that faculae represent the dominate component of the photosphere and are not likely to contribute to a heterogeneity signal.
5. Depending on spot size, we find the stellar contamination signal can be more than $10\times$ larger than transit depth changes expected for atmospheric features in rocky exoplanets. Stellar contamination is most problematic for 1) stars with solar-like spots, 2) early M dwarf spectral types, and 3) molecules such as O_2 with absorption bands at relatively short wavelengths.
6. We show that the stellar contamination is not limited to visual wavelengths but can also be very significant in the near-infrared bands, likely affecting upcoming James Webb Space Telescope spectroscopy of transiting exoplanets. In the case of a transiting Earth-twin, we find unocculted giant spots can alter the strength of planetary absorption features in transmission spectra by $\sim 20\%$ and unocculted spots and faculae can produce features greater than 30 ppm for spectral types M3V and later.
7. We find that stellar spectral contamination across photometric bands due to unocculted starspots with sizes comparable to large sunspot groups can lead to significant errors in radius and therefore density, which may in turn lead to overestimates of planetary volatile content and introduce a stellar-type dependent bias in the density distribution of small planets. This result motivates a possible re-assessment of mass-radius relationships derived from *Kepler* data as well as calls for caution when interpreting upcoming broad-band *TESS* photometry-based exoplanet density measurements.

8. In the case of the TRAPPIST-1 system, we find spot covering fractions $f_{spot} = 8_{-7}^{+18}\%$ to be consistent with the variability reported by Gillon et al. (2016) when considering variability due to both spots and faculae. The associated stellar contamination signals in the optical and near-infrared alter transit depths at wavelengths of interest for planetary atmospheric species by roughly $1-15 \times$ the strength of the planetary feature, significantly complicating James Webb Space Telescope follow-up observations of this system. Similarly, stellar contamination can cause bulk densities of the TRAPPIST-1 planets to be underestimated by $3_{-3}^{+8}\%$, leading to overestimates of their volatile contents.

For TRAPPIST-1 and exciting M dwarf exoplanet hosts in general, tighter constraints on spot and faculae covering fractions are crucial for correct interpretations of high-precision visual and near-infrared transmission spectra from low-mass exoplanets. Stellar contamination is likely to be a limiting factor for detecting biosignatures in transmission spectra of habitable zone planets around M dwarfs. Conversely, exoplanet transit observations in multiple bands can be utilized as a spatial probe to infer the properties of stellar surface

heterogeneities. This is particularly critical to achieving an accurate picture of the evolution of exoplanet system properties from young, active systems to those with older, more quiescent stellar hosts. In preparation for precise *JWST* observations probing for molecular features and potential biosignatures such as oxygen, water, and methane from small exoplanets orbiting M dwarfs, we encourage the community to work towards an equally precise understanding of the stellar photospheres providing the light source for transit observations.

B.R. acknowledges support from the National Science Foundation Graduate Research Fellowship Program under Grant No. DGE-1143953. D.A. acknowledges support from the Max Planck Institute for Astronomy, Heidelberg, for a sabbatical visit. This research has made use of NASA's Astrophysics Data System and the Python modules SciPy, NumPy, and Matplotlib. The results reported herein benefited from collaborations and/or information exchange within NASA's Nexus for Exoplanet System Science (NExSS) research coordination network sponsored by NASA's Science Mission Directorate. The National Solar Observatory is operated by AURA under a cooperative agreement with the National Science Foundation.

REFERENCES

Afram, N., & Berdyugina, S. V. 2015, *A&A*, 576, A34

Andersen, J. M., & Korhonen, H. 2015, *MNRAS*, 448, 3053

Babcock, H. W. 1961, *ApJ*, 133, 572

Barnes, J. R., & Collier Cameron, A. 2001, *MNRAS*, 326, 950

Barnes, J. R., Collier Cameron, A., James, D. J., & Donati, J.-F. 2001, *MNRAS*, 324, 231

Barstow, J. K., & Irwin, P. G. J. 2016, *MNRAS*, 461, L92

Béky, B., Kipping, D. M., & Holman, M. J. 2014, *MNRAS*, 442, 3686

Berdyugina, S. V. 2011, in *Astronomical Society of the Pacific Conference Series*, Vol. 437, Solar Polarization 6, ed. J. R. Kuhn, D. M. Harrington, H. Lin, S. V.

Berdyugina, J. Trujillo-Bueno, S. L. Keil, & T. Rimmele, 219

Berta, Z. K., Charbonneau, D., Bean, J., et al. 2011, *ApJ*, 736, 12

Berta-Thompson, Z. K., Irwin, J., Charbonneau, D., et al. 2015, *Nature*, 527, 204

Bolmont, E., Selsis, F., Owen, J. E., et al. 2017, *MNRAS*, 464, 3728

Brown, T. M. 2001, *ApJ*, 553, 1006

Butler, R. P., Vogt, S. S., Marcy, G. W., et al. 2004, *ApJ*, 617, 580

Carter, J. A., Winn, J. N., Holman, M. J., et al. 2011, *ApJ*, 730, 82

Cauley, P. W., Redfield, S., & Jensen, A. G. 2017, *AJ*, 153, 217

Cram, L. E., & Mullan, D. J. 1979, *ApJ*, 234, 579

Crossfield, I. J. M., & Kreidberg, L. 2017, *ArXiv e-prints*, arXiv:1708.00016

de Wit, J., Wakeford, H. R., Gillon, M., et al. 2016, *Nature*, 537, 69

Désert, J.-M., Sing, D., Vidal-Madjar, A., et al. 2011, *A&A*, 526, A12

Dittmann, J. A., Close, L. M., Green, E. M., & Fenwick, M. 2009, *ApJ*, 701, 756

Dittmann, J. A., Irwin, J. M., Charbonneau, D., et al. 2017, *Nature*, 544, 333

Dravins, D., Ludwig, H.-G., Dahlén, E., & Pazira, H. 2017a, *A&A*, 605, A90

—. 2017b, *A&A*, 605, A91

Fraine, J., Deming, D., Benneke, B., et al. 2014, *Nature*, 513, 526

Giampapa, M. S. 1985, *ApJ*, 299, 781

Gillon, M., Jehin, E., Magain, P., et al. 2011, in European Physical Journal Web of Conferences, Vol. 11, European Physical Journal Web of Conferences, 06002

Gillon, M., Pont, F., Demory, B.-O., et al. 2007, *A&A*, 472, L13

Gillon, M., Jehin, E., Lederer, S. M., et al. 2016, *Nature*, 533, 221

Gillon, M., Triaud, A. H. M. J., Demory, B.-O., et al. 2017, *Nature*, 542, 456

Gondoin, P. 2008, *A&A*, 478, 883

Goulding, N. T., Barnes, J. R., Pinfield, D. J., et al. 2012, *MNRAS*, 427, 3358

Greene, T. P., Line, M. R., Montero, C., et al. 2016, *ApJ*, 817, 17

Hauschildt, P. H., & Baron, E. 1999, *Journal of Computational and Applied Mathematics*, 109, 41

Helling, C., Dehn, M., Woitke, P., & Hauschildt, P. H. 2008a, *The Astrophysical Journal*, 675, L105

Helling, C., & Woitke, P. 2006, *A&A*, 455, 325

Helling, C., Woitke, P., & Thi, W.-F. 2008b, *A&A*, 485, 547

Huitson, C. M., Sing, D. K., Pont, F., et al. 2013, *MNRAS*, 434, 3252

Husser, T.-O., Wende-von Berg, S., Dreizler, S., et al. 2013, *A&A*, 553, A6

Jackson, R. J., & Jeffries, R. D. 2012, *MNRAS*, 423, 2966

—. 2013, *MNRAS*, 431, 1883

Jehin, E., Gillon, M., Queloz, D., et al. 2011, *The Messenger*, 145, 2

Jordán, A., Espinoza, N., Rabus, M., et al. 2013, *ApJ*, 778, 184

Kaltenegger, L., & Traub, W. A. 2009, *The Astrophysical Journal*, 698, 519

Knutson, H. A., Benneke, B., Deming, D., & Homeier, D. 2014, *Nature*, 505, 66

Knutson, H. A., Lewis, N., Fortney, J. J., et al. 2012, *ApJ*, 754, 22

Kopp, G., Lawrence, G., & Rottman, G. 2005, *SoPh*, 230, 129

Kreidberg, L., Bean, J. L., Désert, J.-M., et al. 2014, *Nature*, 505, 69

Llama, J., Jardine, M., Mackay, D. H., & Fares, R. 2012, *MNRAS*, 422, L72

Llama, J., & Shkolnik, E. L. 2015, *ApJ*, 802, 41

—. 2016, *ApJ*, 817, 81

Luger, R., Sestovic, M., Kruse, E., et al. 2017, *Nature Astronomy*, 1, 0129

Mandal, S., Hegde, M., Samanta, T., et al. 2017, *A&A*, 601, A106

Maunder, E. W. 1922, *MNRAS*, 82, 534

McCullough, P. R., Crouzet, N., Deming, D., & Madhusudhan, N. 2014, *ApJ*, 791, 55

Miller-Ricci, E., Seager, S., & Sasselov, D. 2009, *ApJ*, 690, 1056

Morris, B. M., Hebb, L., Davenport, J. R. A., Rohn, G., & Hawley, S. L. 2017, *ApJ*, 846, 99

Narita, N., Fukui, A., Ikoma, M., et al. 2013, *ApJ*, 773, 144

Nascimbeni, V., Mallonn, M., Scandariato, G., et al. 2015, *A&A*, 579, A113

Newton, E. R., Irwin, J., Charbonneau, D., et al. 2017, *ApJ*, 834, 85

Newton, E. R., Irwin, J., Charbonneau, D., Berta-Thompson, Z. K., & Dittmann, J. A. 2016, *ApJL*, 821, L19

Norris, C. M., Beeck, B., Unruh, Y. C., et al. 2017, *A&A*, 605, A45

Nutzman, P., & Charbonneau, D. 2008, *PASP*, 120, 317

Oshagh, M., Santos, N. C., Ehrenreich, D., et al. 2014, *A&A*, 568, A99

Pagano, I., Linsky, J. L., Carkner, L., et al. 2000, *ApJ*, 532, 497

Pont, F., Knutson, H., Gilliland, R. L., Moutou, C., & Charbonneau, D. 2008, *MNRAS*, 385, 109

Pont, F., Sing, D. K., Gibson, N. P., et al. 2013, *MNRAS*, 432, 2917

Rackham, B., Espinoza, N., Apai, D., et al. 2017, *ApJ*, 834, 151

Reiners, A., Basri, G., & Browning, M. 2009, *ApJ*, 692, 538

Ricker, G. R., Winn, J. N., Vanderspek, R., et al. 2015, *Journal of Astronomical Telescopes, Instruments, and Systems*, 1, 014003

Saar, S. H., & Linsky, J. L. 1985, *ApJL*, 299, L47

Sanchis-Ojeda, R., & Winn, J. N. 2011, *ApJ*, 743, 61

Scandariato, G., Nascimbeni, V., Lanza, A. F., et al. 2017, *A&A*, 606, A134

Seager, S., & Sasselov, D. D. 2000, *ApJ*, 537, 916

Shapiro, A. I., Solanki, S. K., Krivova, N. A., et al. 2014, *A&A*, 569, A38

Sing, D. K., Pont, F., Aigrain, S., et al. 2011, *MNRAS*, 416, 1443

Sing, D. K., Fortney, J. J., Nikolov, N., et al. 2016, *Nature*, 529, 59

Sullivan, P. W., Winn, J. N., Berta-Thompson, Z. K., et al. 2015, *ApJ*, 809, 77

Tregloan-Reed, J., Southworth, J., & Tappert, C. 2013, *MNRAS*, 428, 3671

Vida, K., Kővári, Z., Pál, A., Oláh, K., & Kriskovics, L. 2017, *ApJ*, 841, 124

Wheatley, P. J., Louden, T., Bourrier, V., Ehrenreich, D., & Gillon, M. 2017, *MNRAS*, 465, L74

Winn, J. N., Petigura, E. A., Morton, T. D., et al. 2017, ArXiv e-prints, arXiv:1710.04530

Witte, S., Helling, C., Barman, T., Heidrich, N., & Hauschildt, P. 2011, *A&A*, 529, A44

Witte, S., Helling, C., & Hauschildt, P. H. 2009, *A&A*, 506, 1367

Woitke, & Helling. 2003, *A&A*, 399, 297

Woitke, P., & Helling, C. 2004, *A&A*, 414, 335

Wolf, E. T. 2017, *ApJL*, 839, L1

Zellem, R. T., Griffith, C. A., Pearson, K. A., et al. 2015, *ApJ*, 810, 11

Zellem, R. T., Swain, M. R., Roudier, G., et al. 2017, *ApJ*, 844, 27

Zeng, L., Sasselov, D. D., & Jacobsen, S. B. 2016, *ApJ*, 819, 127